

Moderní experimentální metody

Rentgenová a elektronová spektroskopie I

Spektroskopie absorpční hrany rtg záření

- Principy, experimentální realizace
- Metody: XANES, EXAFS
- Postupy vyhodnocení dat, příklady
- Magnetismus – XMCD
- RIXS

Moderní experimentální metody

Rentgenová a elektronová spektroskopie II

Anomální rtg difrakce

- Kramersovy-Kronigovy relace
- Anomální difrakce – principy, použití
- DAES

Flurescenční spektroskopie

- Spektroskopie charakteristického záření (XRF, EDS, WDS)
- Kvalitativní a kvantitativní analýza
- TRXRF
- Fluorescence ve stojaté vlně (SW-XRF) – rtg reflexe, difrakce

Moderní experimentální metody

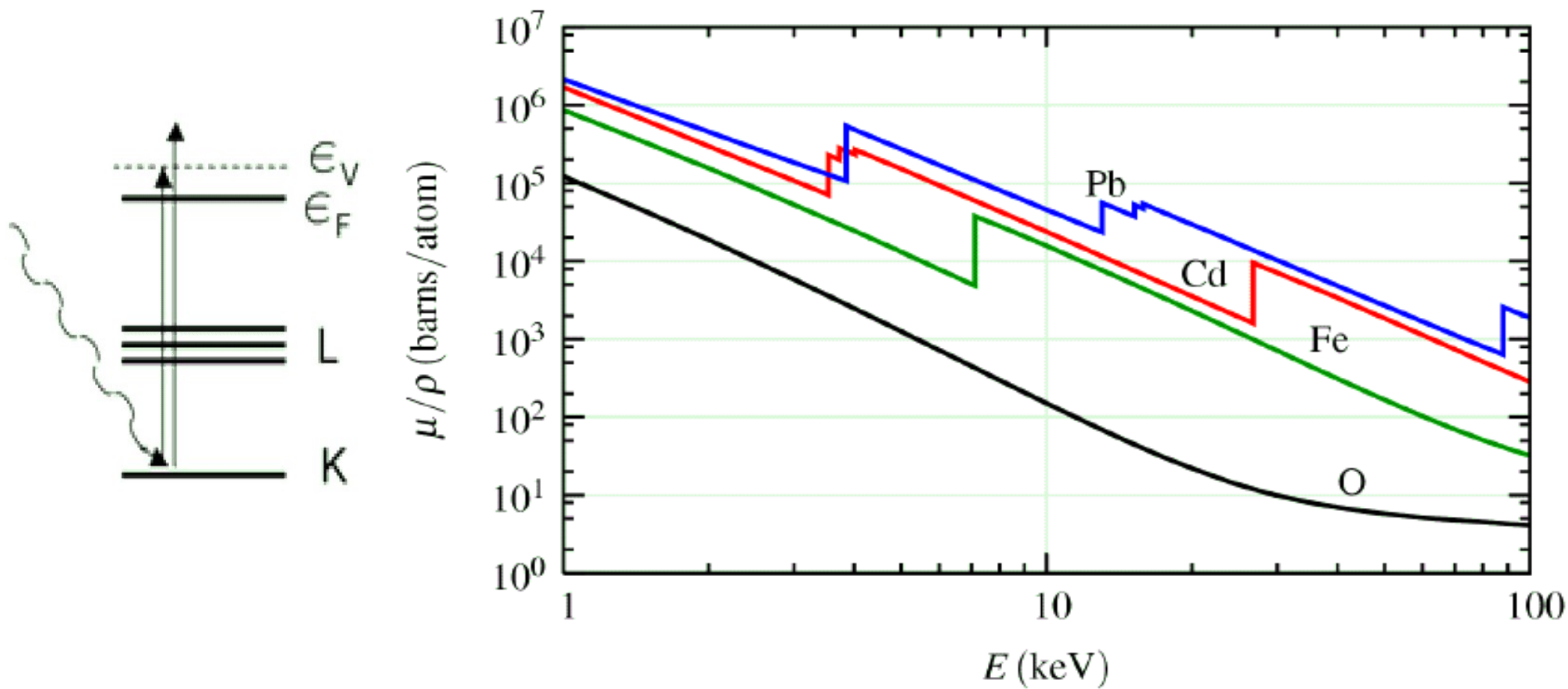
Rentgenová a elektronová spektroskopie III

Fotoelektronová spektroskopie

- Fotoelektronová spektroskopie (XPS) a spektroskopie Augerových elektronů (AES)
- Úhlově rozlišená fotoelektronová spektroskopie (ARPES)
- Experimentální aspekty
- Zdroje: ARPES, ARUPS
- Detektory
- Příprava vzorků

Absorpce rtg záření

Ionizace hluboké elektronové hladiny – absorpční hrana.



Závislost absorpce na vlnové délce pro olovo ($Z=82$).

Empirická závislost absorpce na energii
mimo absorpční hranu:

$$\alpha(\epsilon) = \frac{a}{\epsilon^3} + \frac{b}{\epsilon^4},$$

Index lomu pro rtg

- Filtrace záření – Ni filtr pro Cu, buď jako vrstva různé tloušťky, nebo v multivrstvě
- $n(\lambda) = 1 - \delta(\lambda) = 1 - \delta'(\lambda) + i\beta(\lambda)$
- Indexu lomu: reálná část – refrakce
 imaginární část – absorpcie
- $E = E_0 \exp(iKn r) = E_0 \exp(iKr) \exp(-iK\delta' r) \exp(-K\beta r)$
- Intenzita při absorpci:
 $I = I_0 \exp(-\mu z) = |E|^2 = I_0 \exp(-2K\beta z)$
 $\mu(\lambda) = 4\pi\beta(\lambda) / \lambda$

X-ray optical properties

Dielectric function (Drude):

$$\epsilon(\omega) = 1 - ne^2/[\epsilon_0 m \omega (\omega + i/\tau)]$$

High frequency limit:

$$\epsilon(\omega) \approx 1 - ne^2/[\epsilon_0 m_e \omega^2]$$

$$\epsilon(\omega) \approx 1 - NZr_e \lambda^2 / \pi < 1$$

$$r_e = e^2 / [4\pi \epsilon_0 m_e c^2] = 2.8179 \cdot 10^{-15} \text{ m}$$

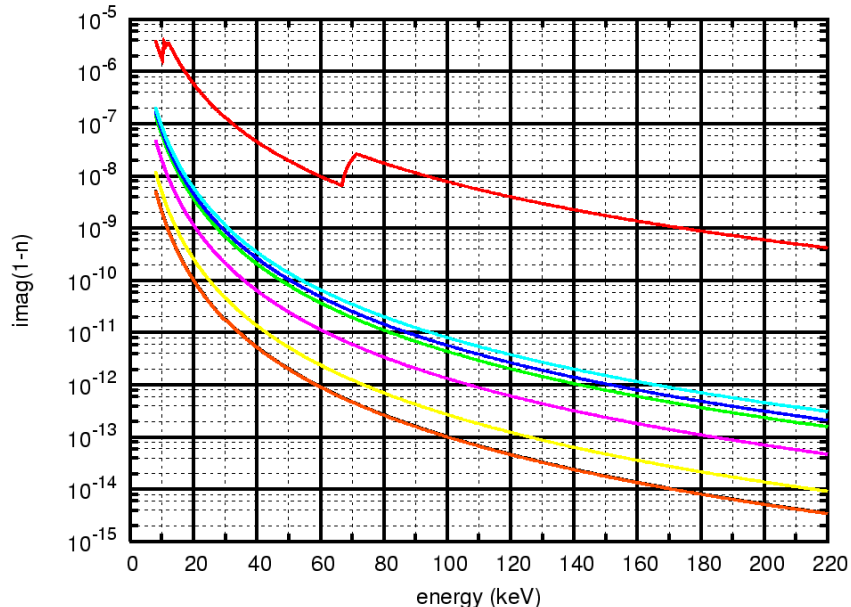
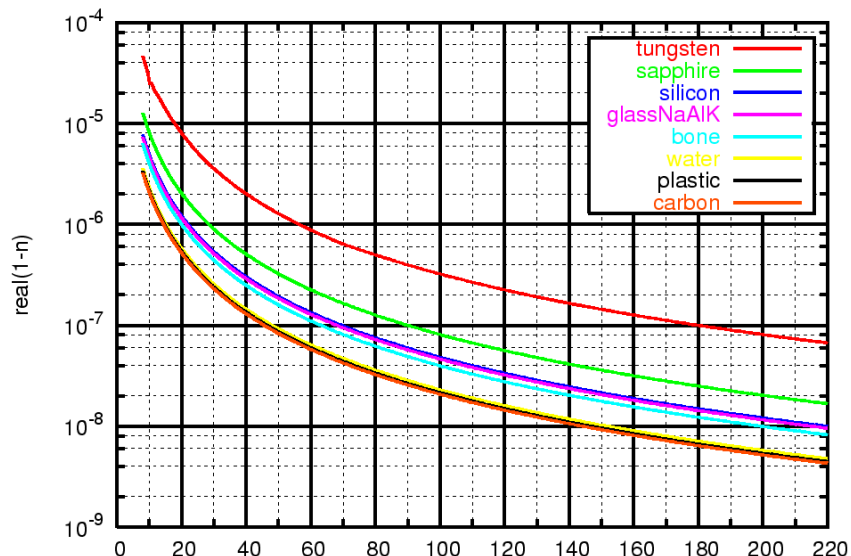
$$n = 1 - \delta + i\beta = 1 - (\delta_0 - i\beta_0) \rho_{\text{rel}}$$

$$\delta \approx -NZr_e \lambda^2 / \pi$$

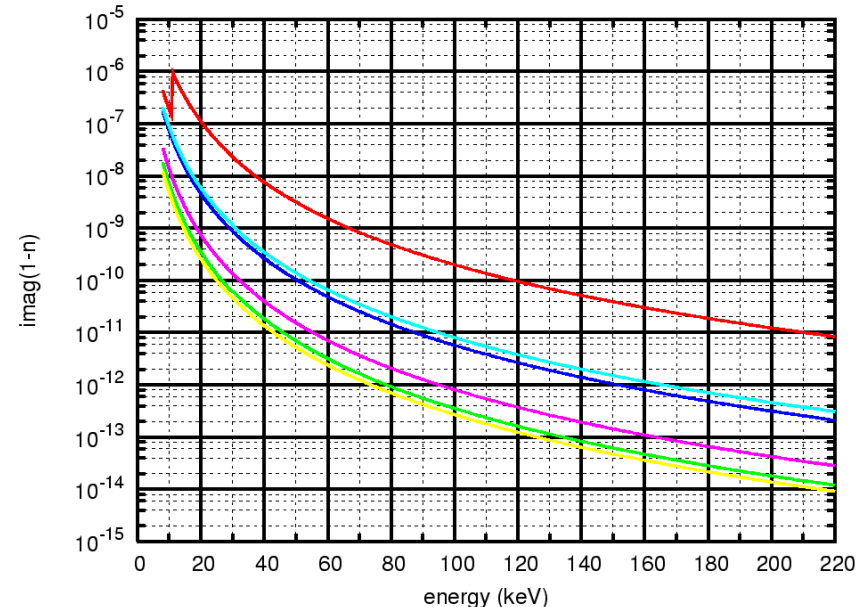
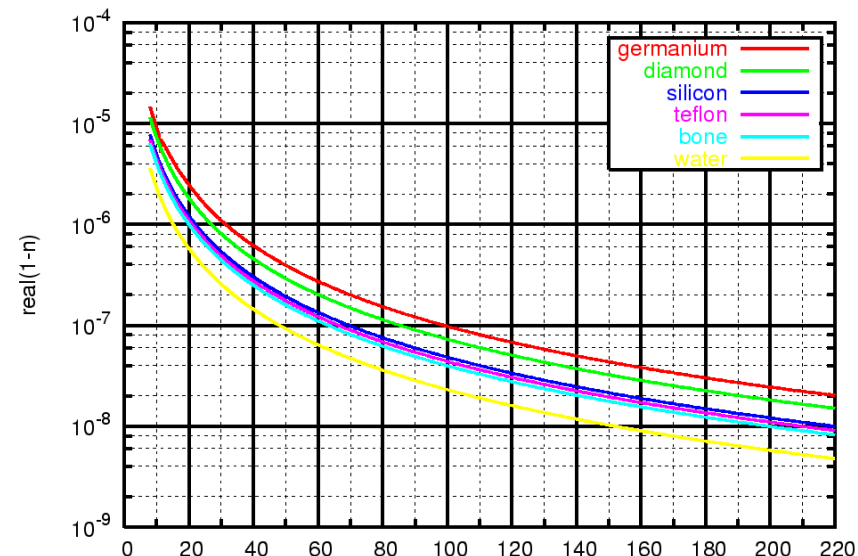
Electron density = proton density \sim mass density

Dekrement indexu lomu $\delta(E)=1-n(E)$: závislost reálné a imaginární části na energii

Reálná
část
 $\delta \sim E^{-2}$

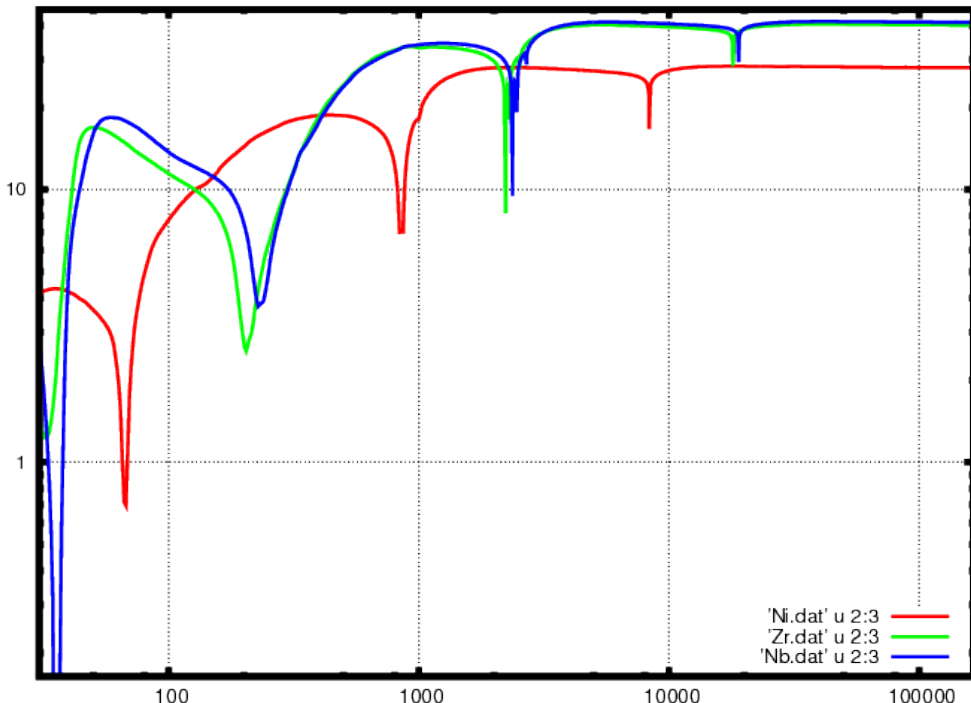


Imaginární
část
 $\delta \sim E^{-3}$
→ Dávka
z ozáření
klesá!

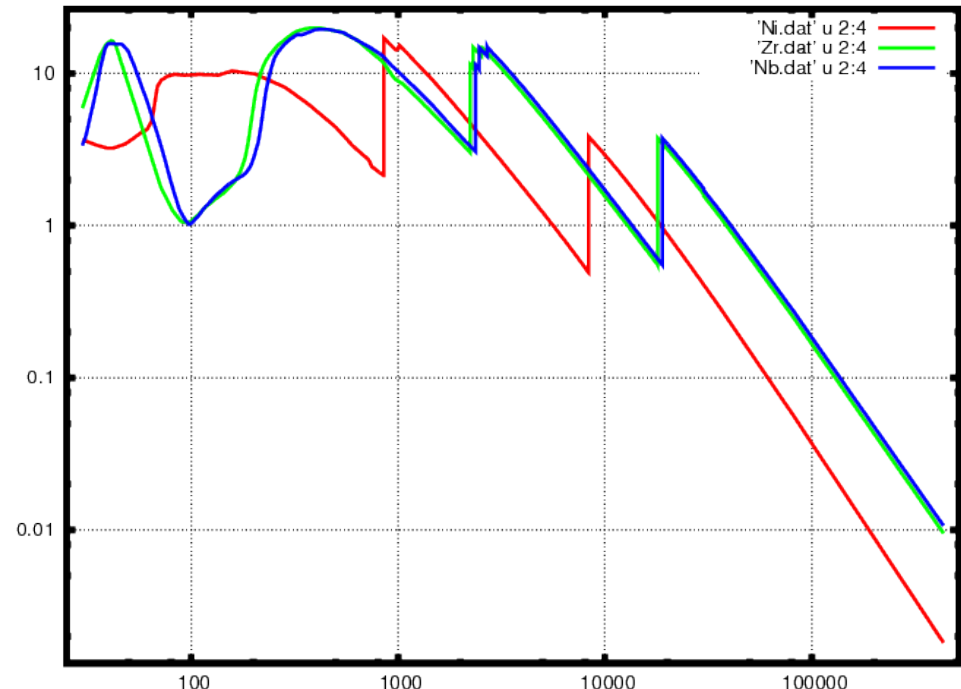


Atomový strukturní faktor $f(E) = Z + f_1(E) + i f_2(E)$:

log-log závislost f_1



a f_2 na energii



Výpočet: a.s.f. pro všechny atomy ve vzorci nebo elementární buňce
 → strukturní faktor → susceptibilita → index lomu

Dopředná vlna – jeden atom:

$$E^{\text{forw}} = f(r_e/r) E^{\text{inc}}$$

Vlnový vektor:

$$\mathbf{k}(\mathbf{r}) = n(\mathbf{r}) \mathbf{K}, \quad K = 2\pi/\lambda$$

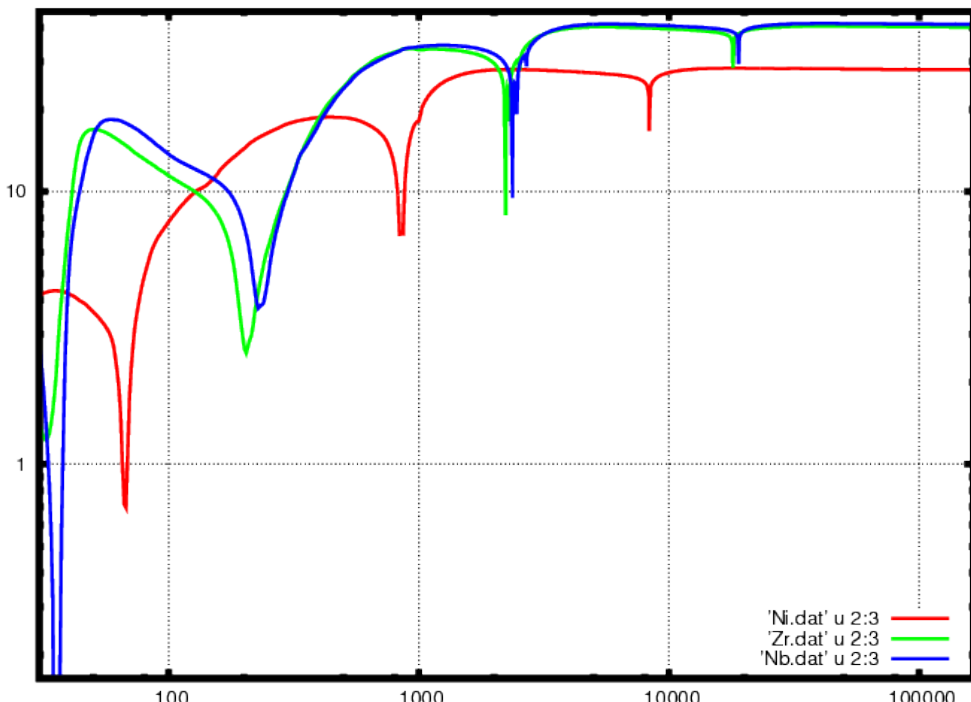
$$\rho_{\text{el}} = \text{suma}(f) / V_{\text{elem.b.}}$$

$$\chi = - (r_{\text{el}} \lambda^2 / \pi) \rho_{\text{el}}$$

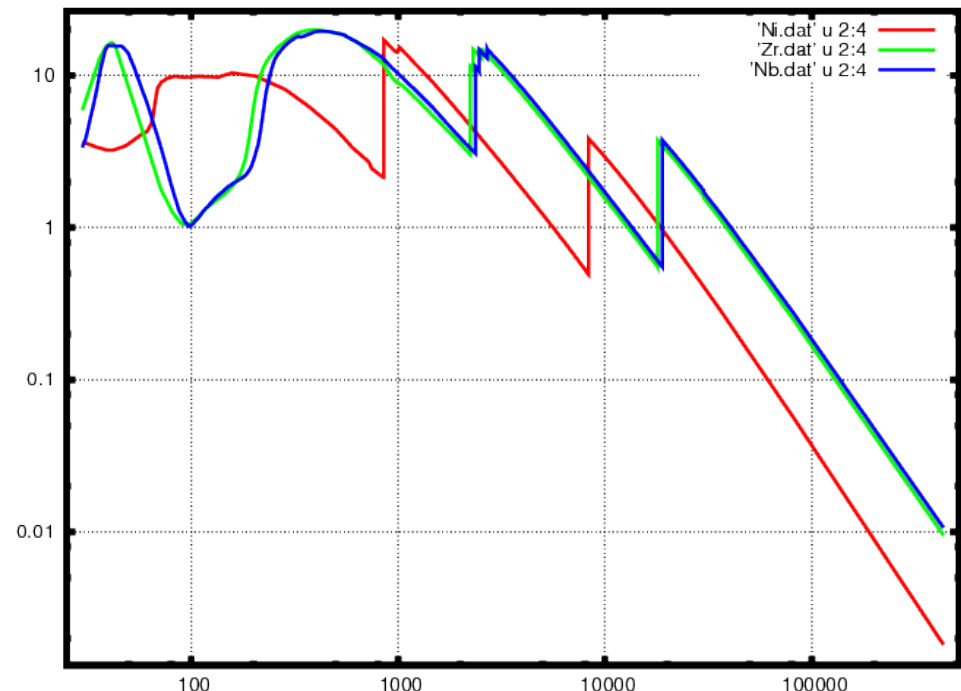
$$n^2 = \epsilon_r = 1 + \chi \rightarrow \delta = -\chi/2$$

Atomový strukturní faktor $f(E) = Z + f_1(E) + i f_2(E)$:

log-log závislost f_1



a f_2 na energii



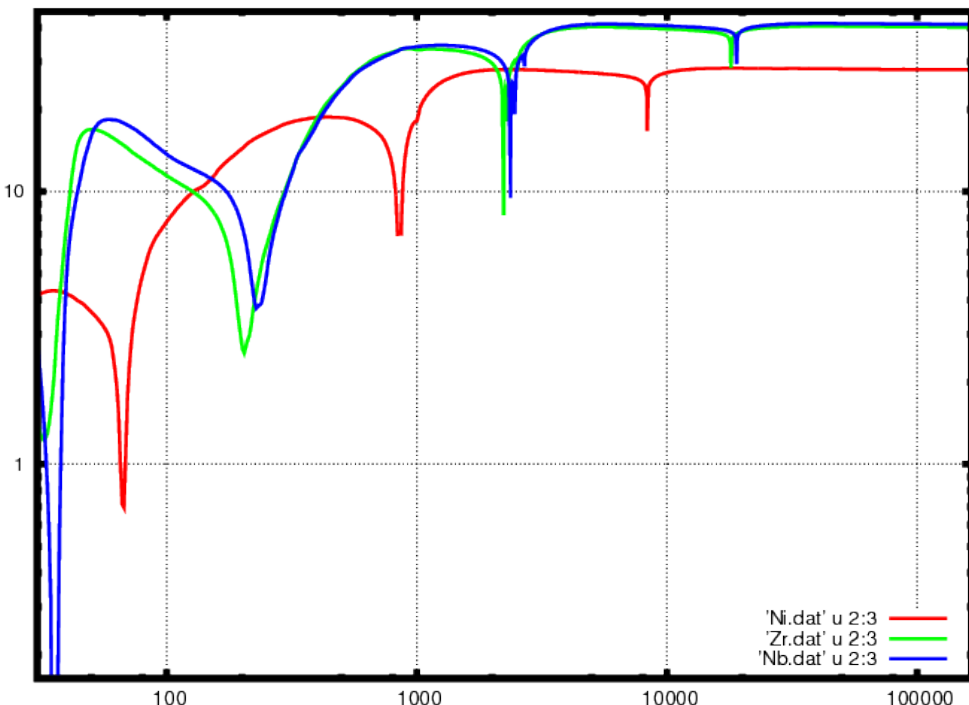
$$f''(E) = \left(\frac{mcE}{2e^2\hbar} \right) \sigma(E)$$

$$f'(E_0) = \frac{2}{\pi} \int_0^\infty \frac{E f''(E)}{(E_0^2 - E^2)} dE$$

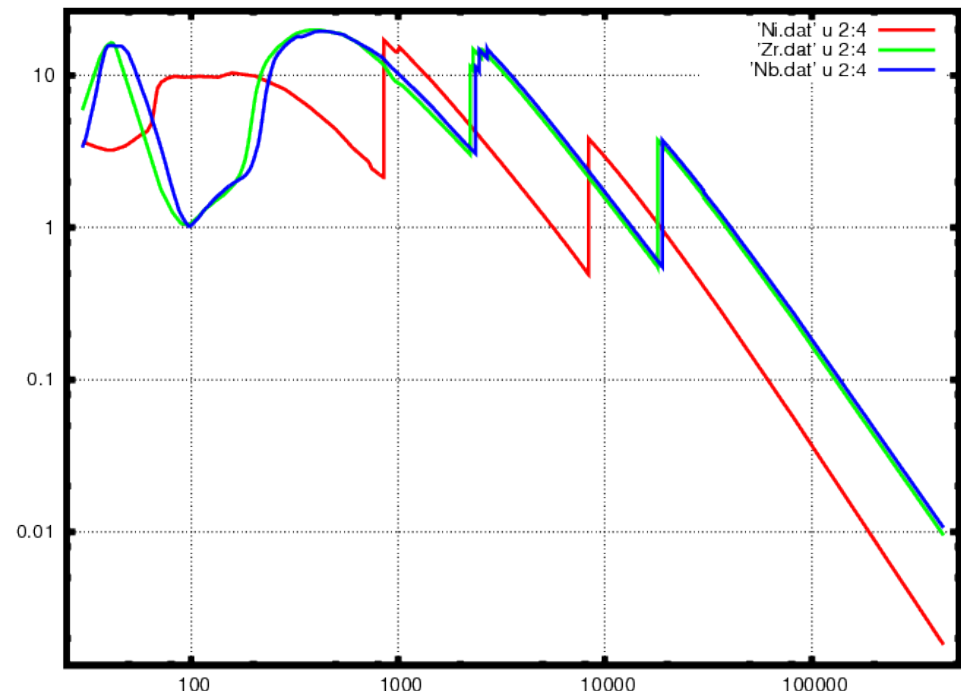
$$f''(E_0) = -\frac{2E_0}{\pi} \int_0^\infty \frac{f'(E)}{(E_0^2 - E^2)} dE$$

Atomový strukturní faktor $f(E) = Z + f_1(E) + i f_2(E)$:

log-log závislost f_1



a f_2 na energii



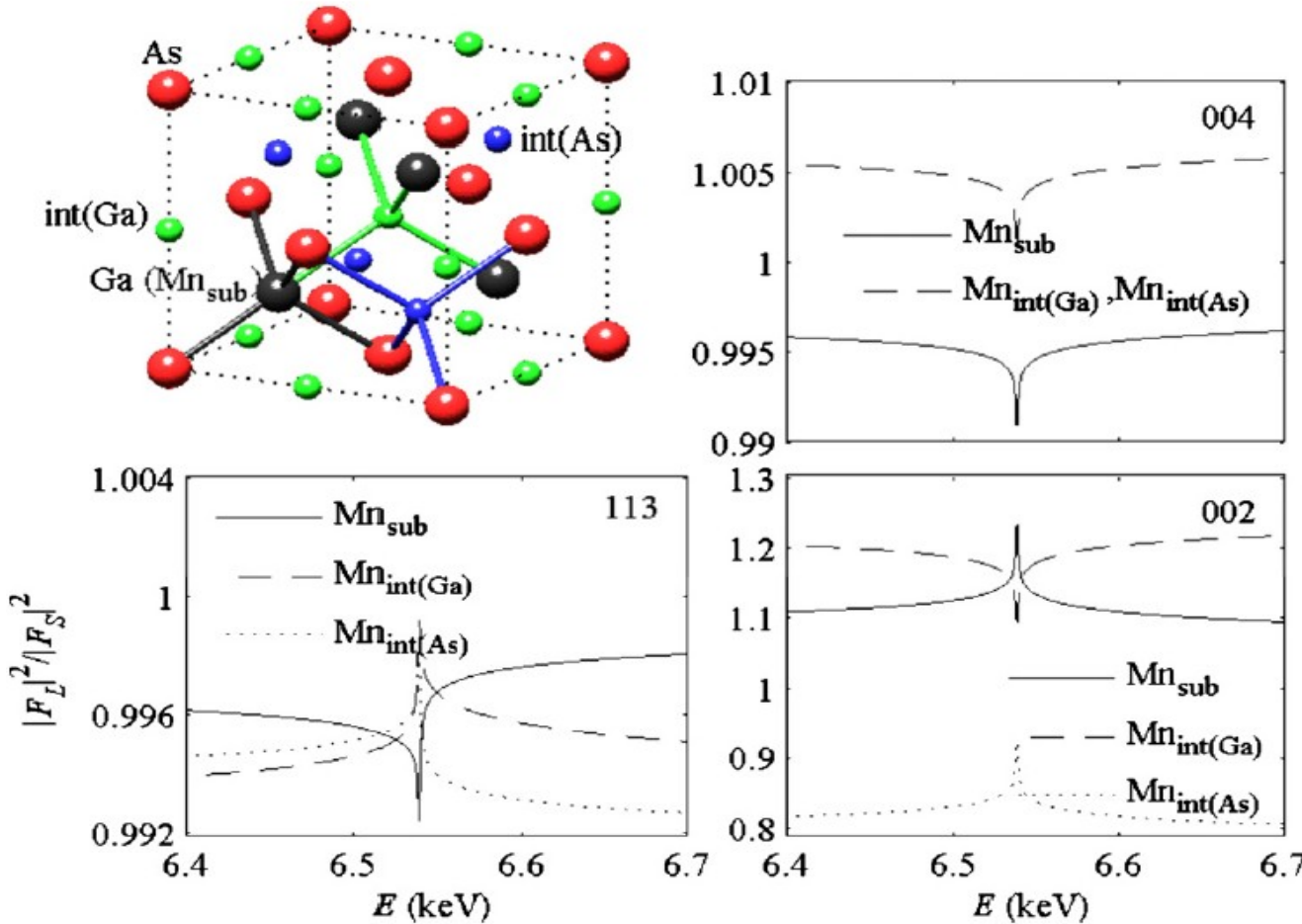
Difrakce: atomový rozptylový faktor se obvykle approximuje jako

$$f_{at}(Q, E) = f_0(Q) + f_1(E) + i f_2(E)$$

$$F = \sum_n f_n(Q, E) e^{i Q \cdot r_n}$$

Anomální rtg difrakce

$$F(\mathbf{h}) = 4\{(1 - c_{\text{sub}})f_{\text{Ga}}(\mathbf{h}) + c_{\text{sub}}f_{\text{Mn}}(\mathbf{h}) + \phi(\mathbf{h})f_{\text{As}}(\mathbf{h}) \\ + (-1)^h f_{\text{Mn}}(\mathbf{h})[c_{\text{int(As)}} + c_{\text{int(Ga)}}\phi(\mathbf{h})]\},$$

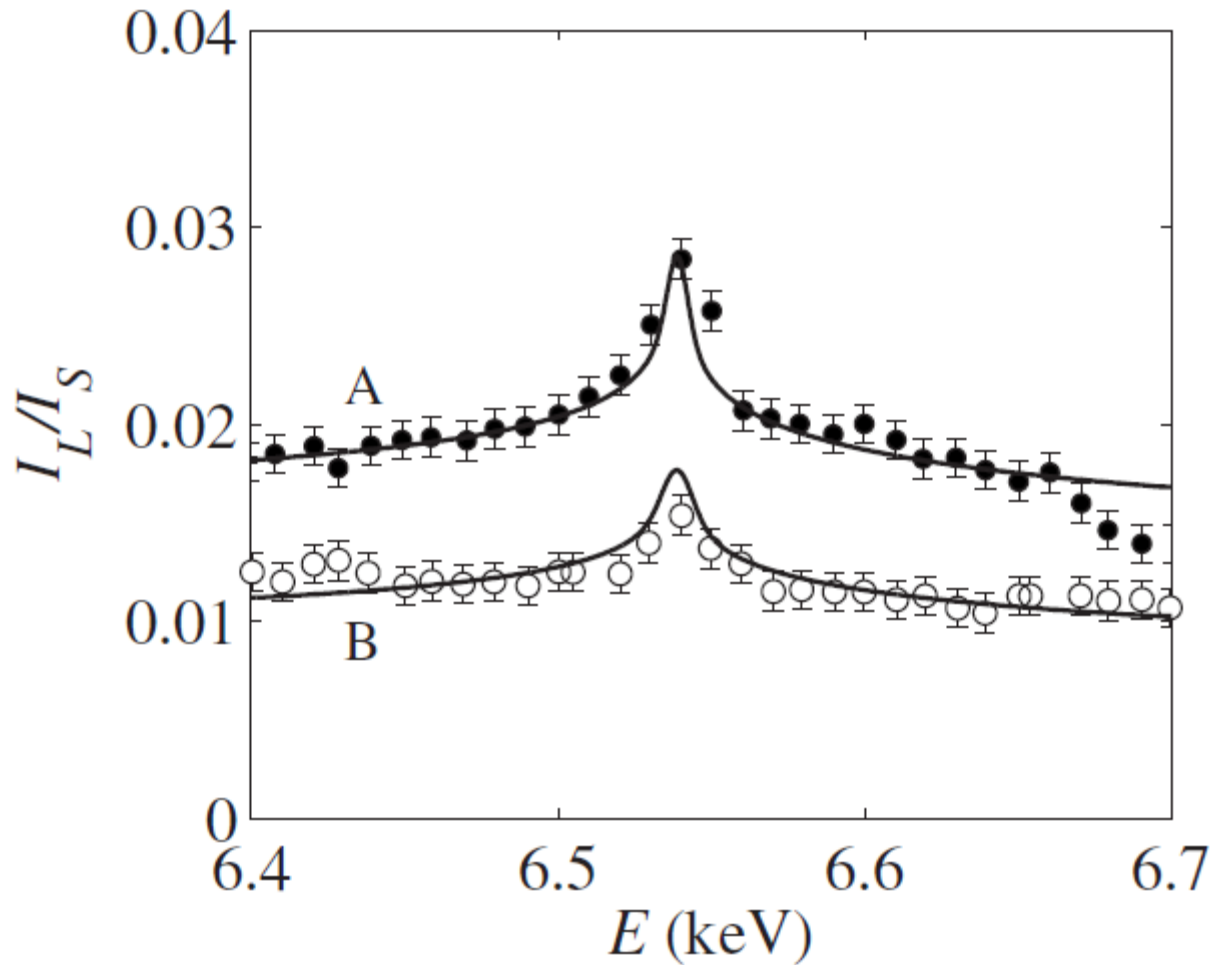


APPLIED PHYSICS LETTERS 97, 181913 (2010)

Density of Mn interstitials in (Ga,Mn)As epitaxial layers determined by anomalous x-ray diffraction

V. Holý,^{1,a)} X. Martí,¹ L. Horák,¹ O. Caha,² V. Novák,³ M. Cukr,³ and T. U. Schülli⁴

Anomální rtg difrakce



From the fit we obtained for all values of n the following concentrations $c_{\text{sub}} = (8.2 \pm 1.1)\%$, $(c_{\text{int(As)}} - c_{\text{int(Ga)}})^{(A)} = (1.6 \pm 0.3)\%$, and $(c_{\text{int(As)}} - c_{\text{int(Ga)}})^{(B)} = (2.4 \pm 0.3)\%$. Fortu-

Anomální rtg difrakce

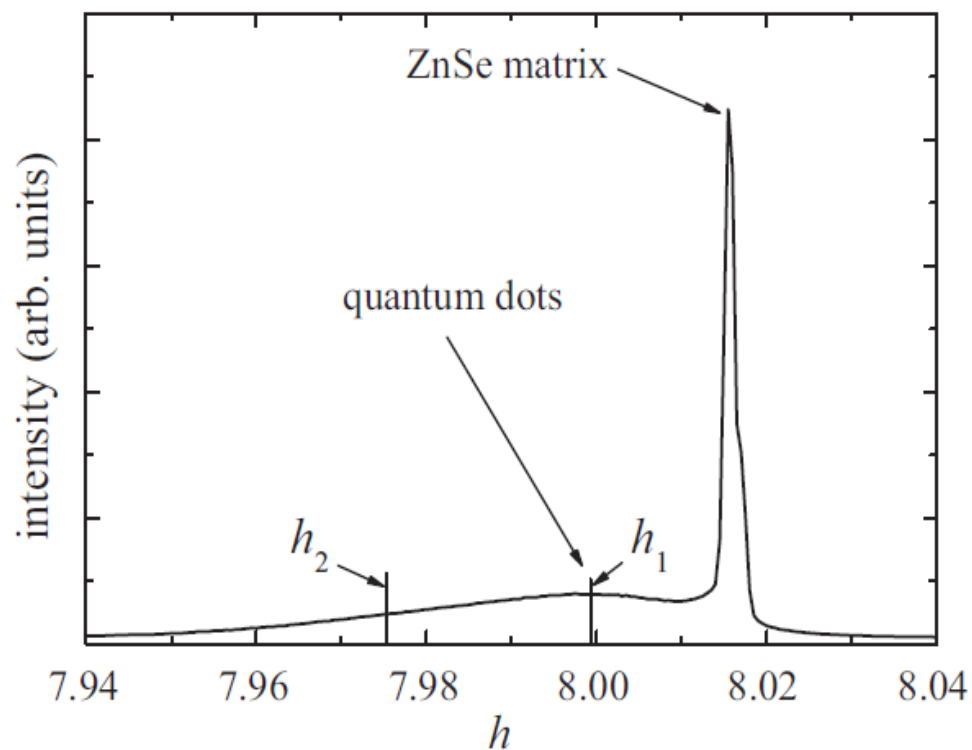


Fig. 3. The diffraction profile measured in radial (800) direction. The h_1 and h_2 indicate the radial positions in reciprocal space where the DAES data were collected.

Complementary information on CdSe/ZnSe quantum dot local structure from extended X-ray absorption fine structure and diffraction anomalous fine structure measurements

Journal of Alloys and Compounds 523 (2012) 155–160

Anomální rtg difrakce

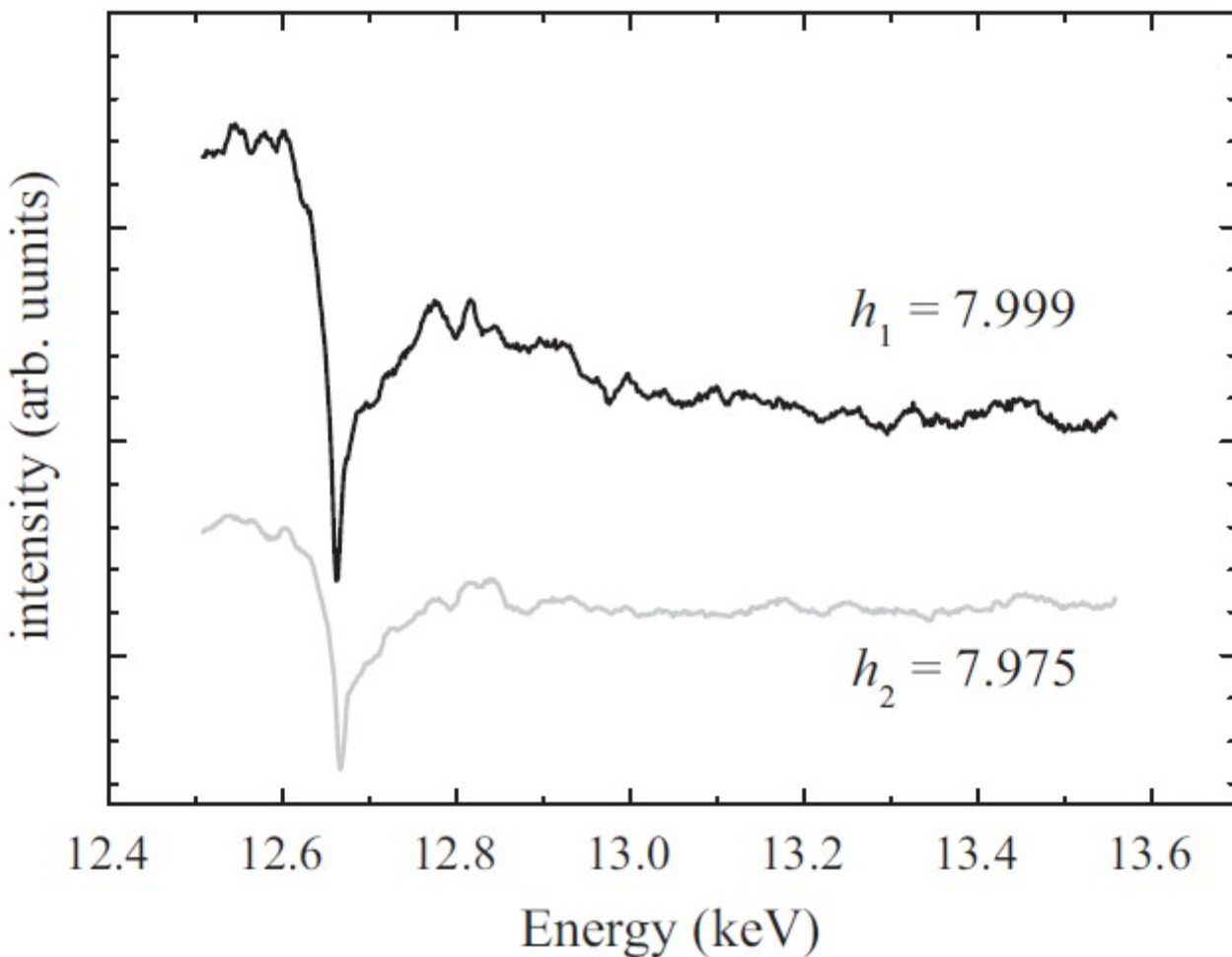


Fig. 4. Raw DAES spectra collected at the Se K-edge at two different values of h indicated in Fig. 3.

Complementary information on CdSe/ZnSe quantum dot local structure from extended X-ray absorption fine structure and diffraction anomalous fine structure measurements

Journal of Alloys and Compounds 523 (2012) 155–160

Anomální rtg difrakce

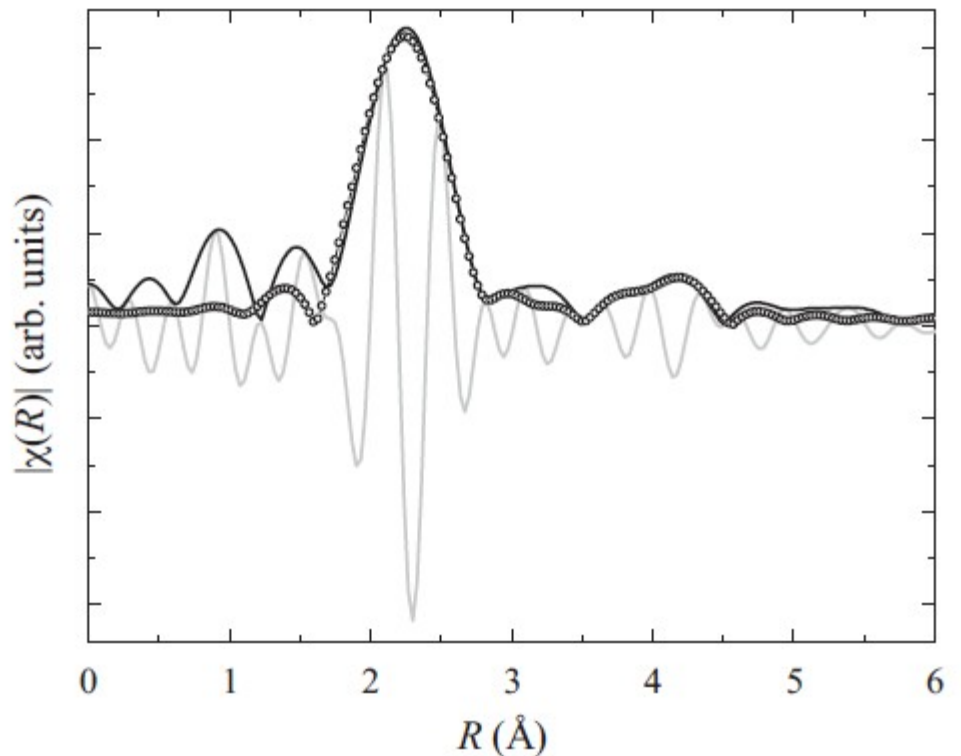
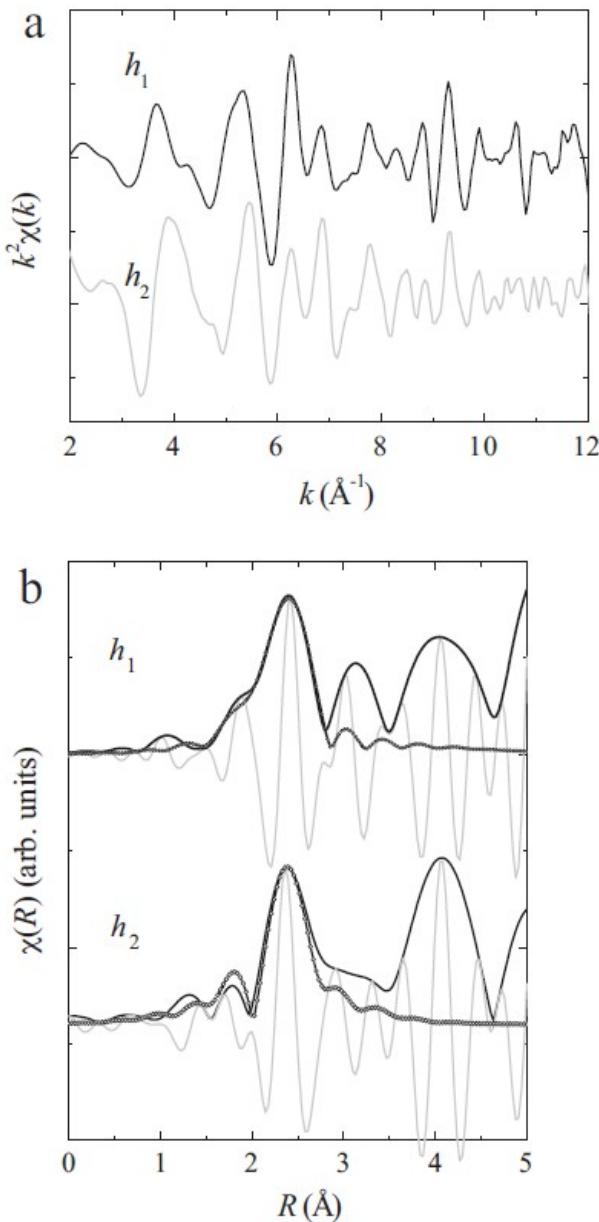


Fig. 2. The magnitude (black line) and the real part (grey line) of the Fourier transformation of the EXAFS oscillations presented in Fig. 1 and the best fit (circles) of the first and second coordination shells for CdSe quantum dots.

Complementary information on CdSe/ZnSe quantum dot local structure from extended X-ray absorption fine structure and diffraction anomalous fine structure measurements

E. Piskorska-Hommel^{a,b,*}, V. Holý^c, O. Caha^d, A. Wolska^b, A. Gust^a, C. Kruse^a, H. Kröncke^a, J. Falta^a, D. Hommel^a

Journal of Alloys and Compounds 523 (2012) 155–160

Anomální rtg difrakce

Table 1

The EXAFS and DAFS fitting results determined for Cd and Se K-edge, respectively. R are the distances between the absorbing atom and its near-neighbors, N is the coordination number, σ^2 is the Debye–Waller factor, respectively.

	EXAFS (Cd K-edge; 2 shells)		DAFS (Se K-edge; one shell)	
	CdSe	Sample	h_1	h_2
N_{Se}	4	4	–	–
N_{Cd}	12	5 (2)	1.6 (0.4)	2.8 (0.8)
N_{Zn}	–	7 (2)	2.4 (0.4)	1.2 (1)
$R_{\text{Cd-Se}} (\text{\AA})$ (2.62)	2.62 (0.01)	2.61 (0.01)	2.62 (0.02)	2.54 (0.03)
$R_{\text{Cd-Cd}} (\text{\AA})$ (4.28)	4.31 (0.02)	4.37 (0.02)	–	–
$R_{\text{Cd-Zn}} (\text{\AA})$ (4.01)	–	4.18 (0.04)	–	–
$R_{\text{Se-Zn}} (\text{\AA})$ (2.45)	–	–	2.45 (0.02)	2.45 (0.03)
$\sigma^2_{\text{Cd-Se}} (\text{\AA}^2)$	0.003 (0.001)	0.002 (0.001)	0.004 (0.002)	0.009 (0.003)
$\sigma^2_{\text{Cd-Cd}} (\text{\AA}^2)$	0.014 (0.002)	0.012 (0.005)	–	–
$\sigma^2_{\text{Cd-Zn}} (\text{\AA}^2)$	–	0.015 (0.003)	–	–
$\sigma^2_{\text{Se-Zn}} (\text{\AA}^2)$	–	–	0.008 (0.005)	0.023 (0.009)

Complementary information on CdSe/ZnSe quantum dot local structure from extended X-ray absorption fine structure and diffraction anomalous fine structure measurements

Journal of Alloys and Compounds 523 (2012) 155–160

E. Piskorska-Hommel^{a,b,*}, V. Holý^c, O. Caha^d, A. Wolska^b, A. Gust^a, C. Kruse^a, H. Kröncke^a, J. Falta^a, D. Hommel^a

Anomální rtg difrakce

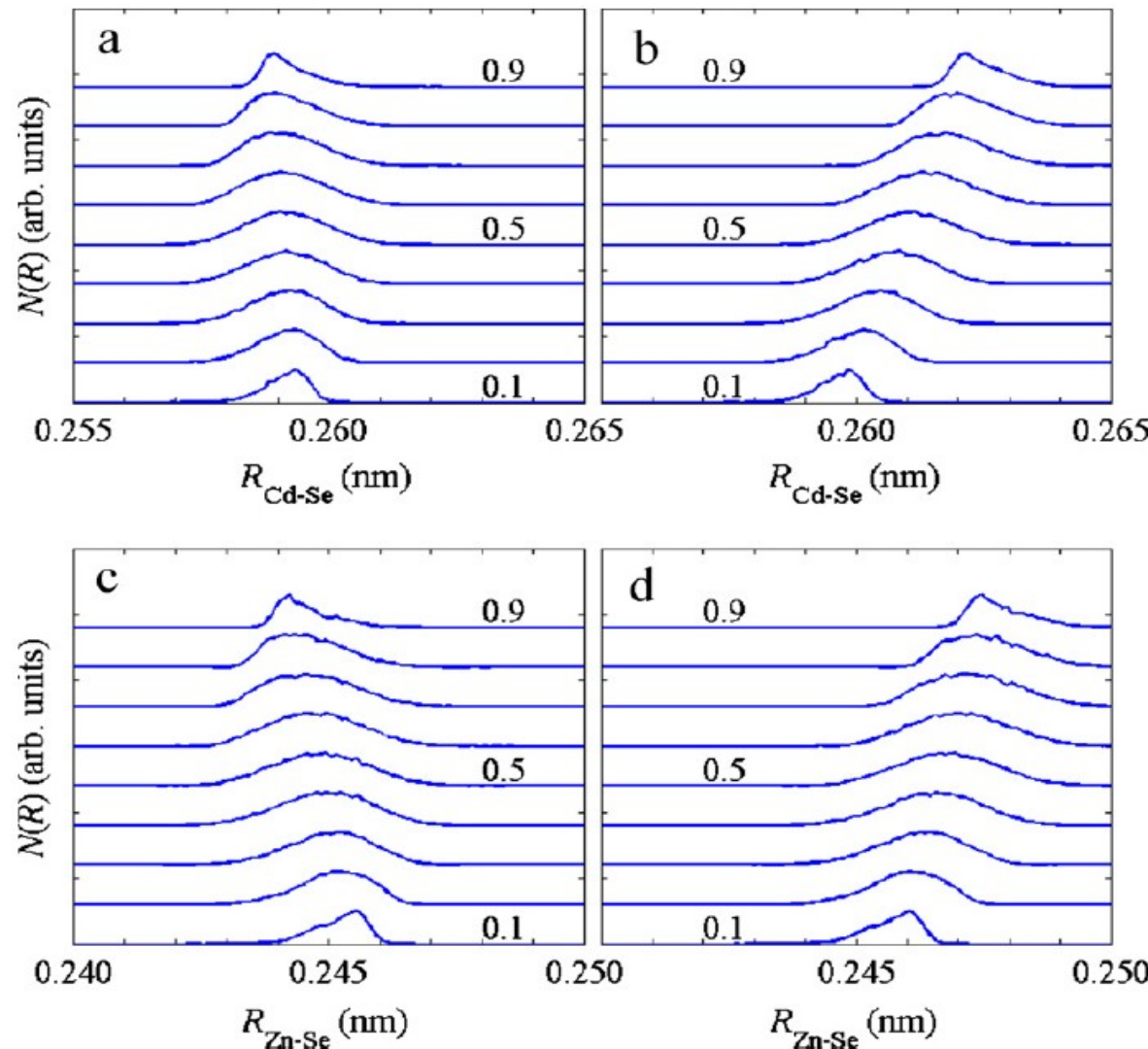


Fig. 6. The distribution of the Cd–Se (a and b) and Zn–Se (c and d) bond lengths calculated by the valence-field model assuming fully relaxed (b and d) and biaxially strained (a and c) $\text{Cd}_x\text{Zn}_{1-x}\text{Se}$ lattice (see the text for details). The parameter of the curves is the concentration x of Cd. The curves are shifted vertically for clarity.

Complementary information on CdSe/ZnSe quantum dot local structure from extended X-ray absorption fine structure and diffraction anomalous fine structure measurements

Journal of Alloys and Compounds 523 (2012) 155–160

Vznik charakteristického rtg záření

Přechody mezi hlubokými elektronovými hladinami ($Z>3$)

Výběrová pravidla: $\Delta n \neq 0$, $\Delta l = \pm 1$, $\Delta j = 0, \pm 1$

Energie přechodu: $\epsilon_{fi} = \hbar\omega = Ry(Z - \sigma_f)^2 \left(\frac{1}{n_f^2} - \frac{1}{n_i^2} \right)$

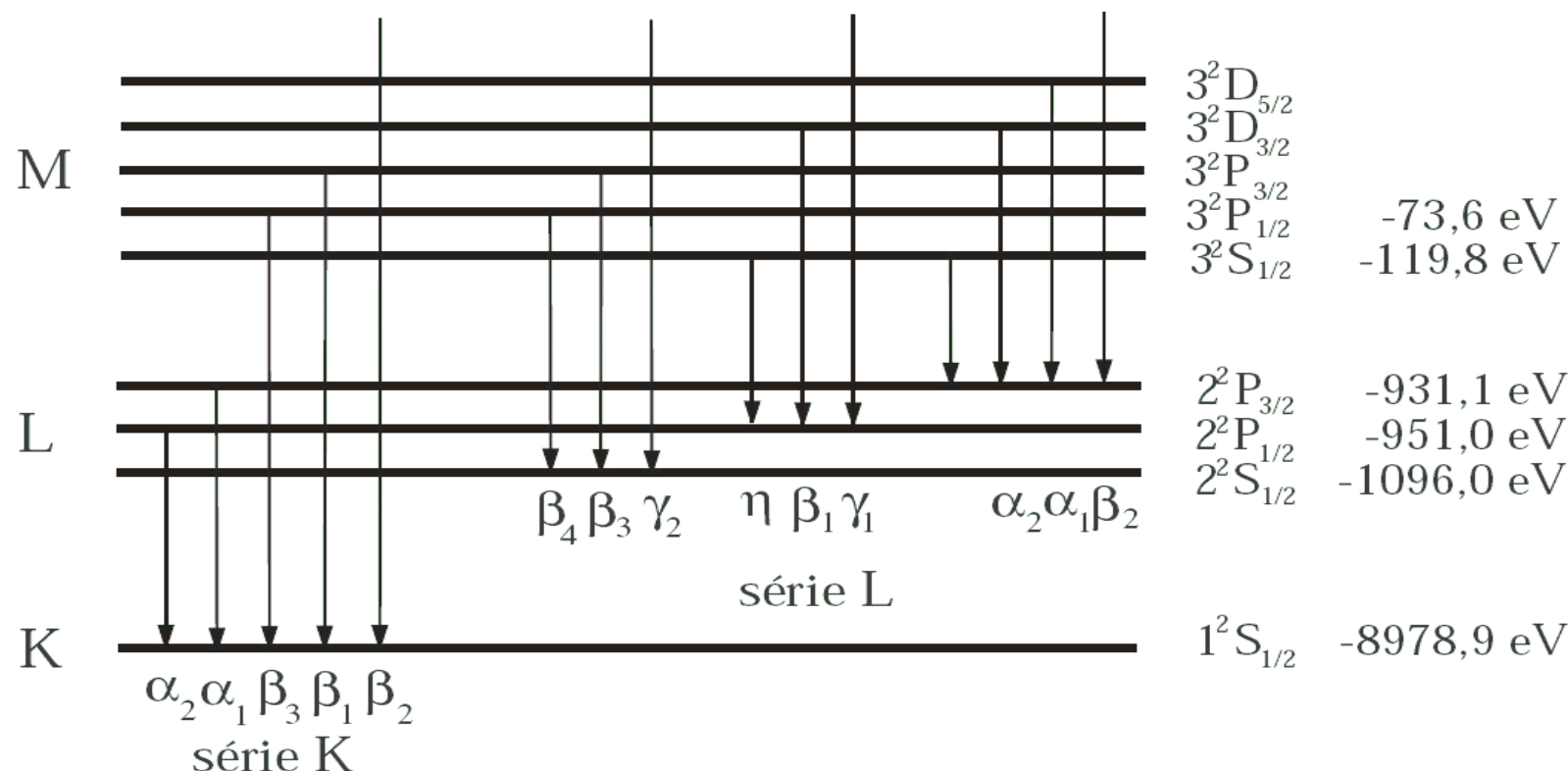
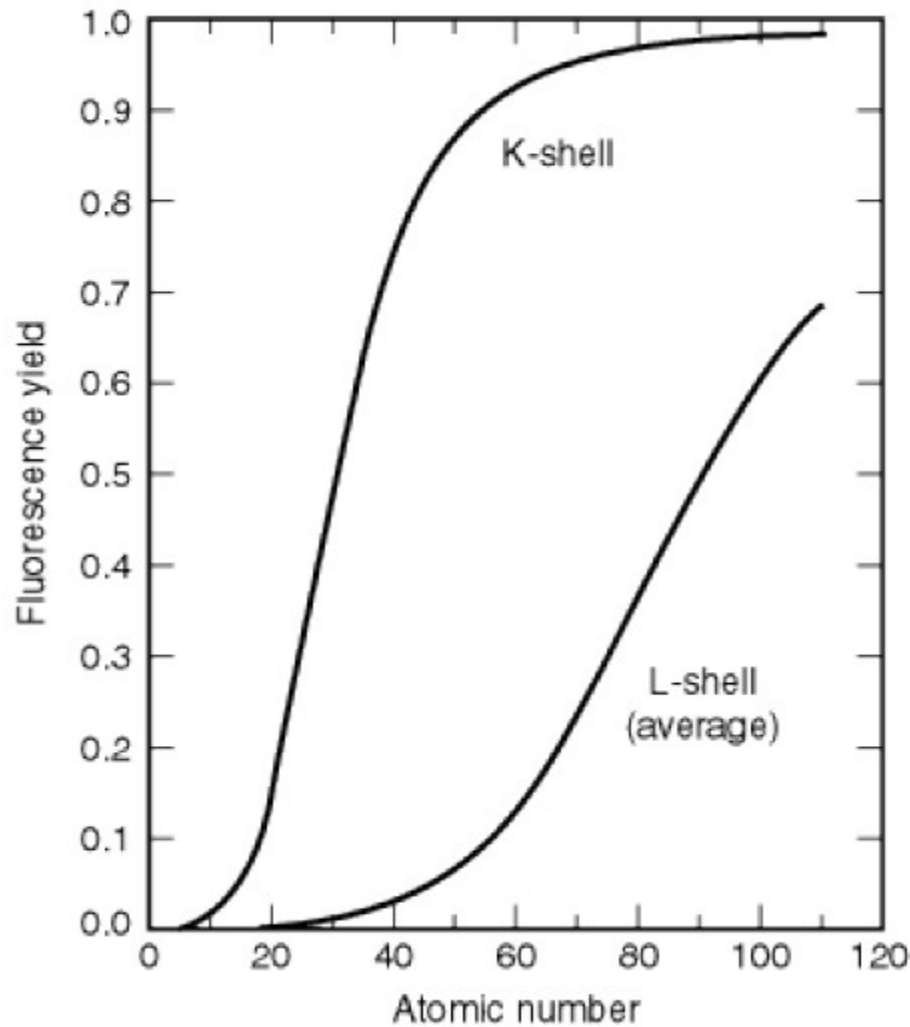


Schéma přechodů pro měď ($Z=29$).

Charakteristické rtg záření



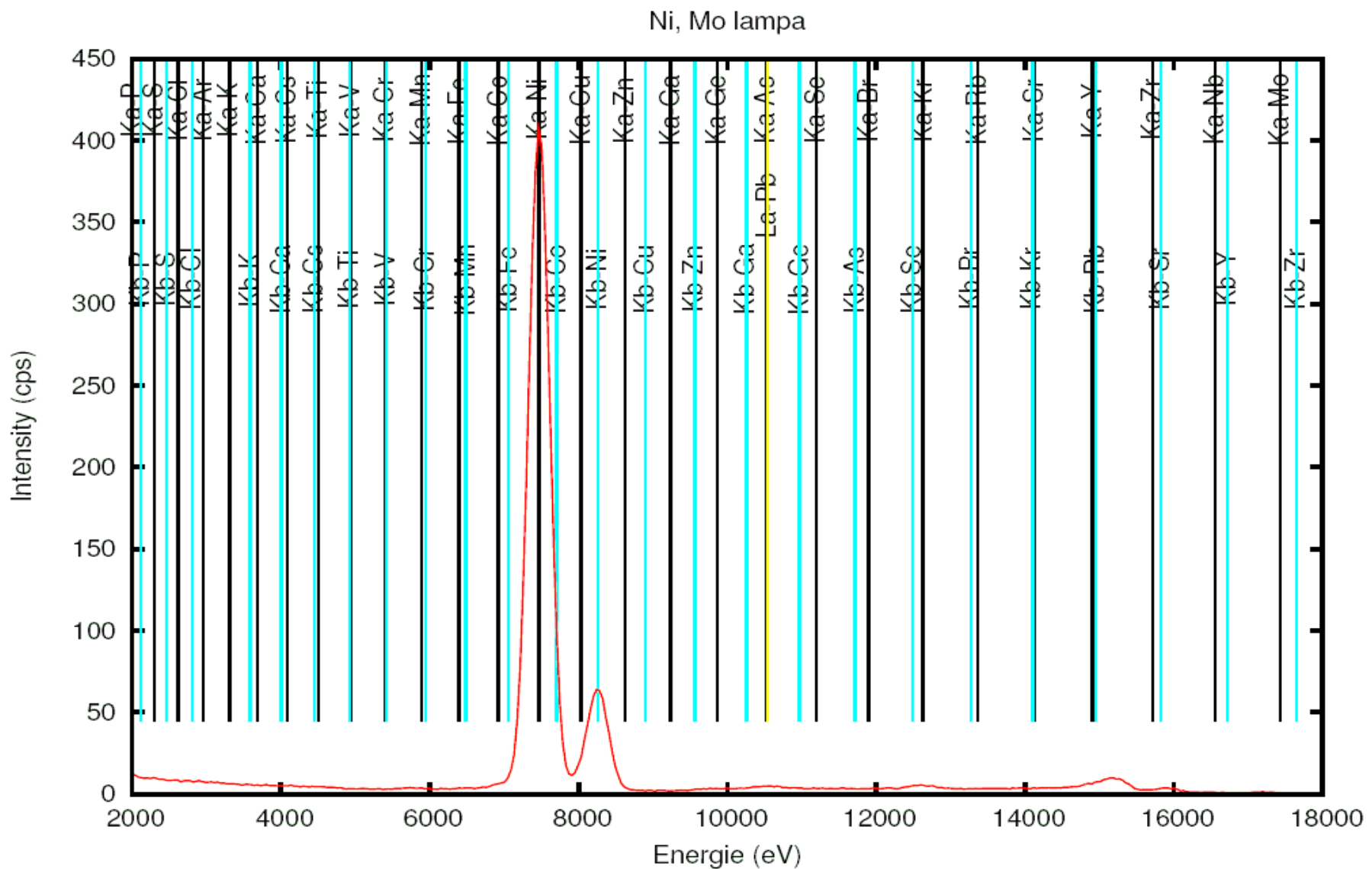
XRF

Rentgenová fluorescenční spektroskopie

X-ray Fluorescence spectroscopy – XRF

Ionizace atomů vzorku rtg svazkem a měření spektra

sekundárního rtg záření. Nezávisí na chemickém stavu atomu.



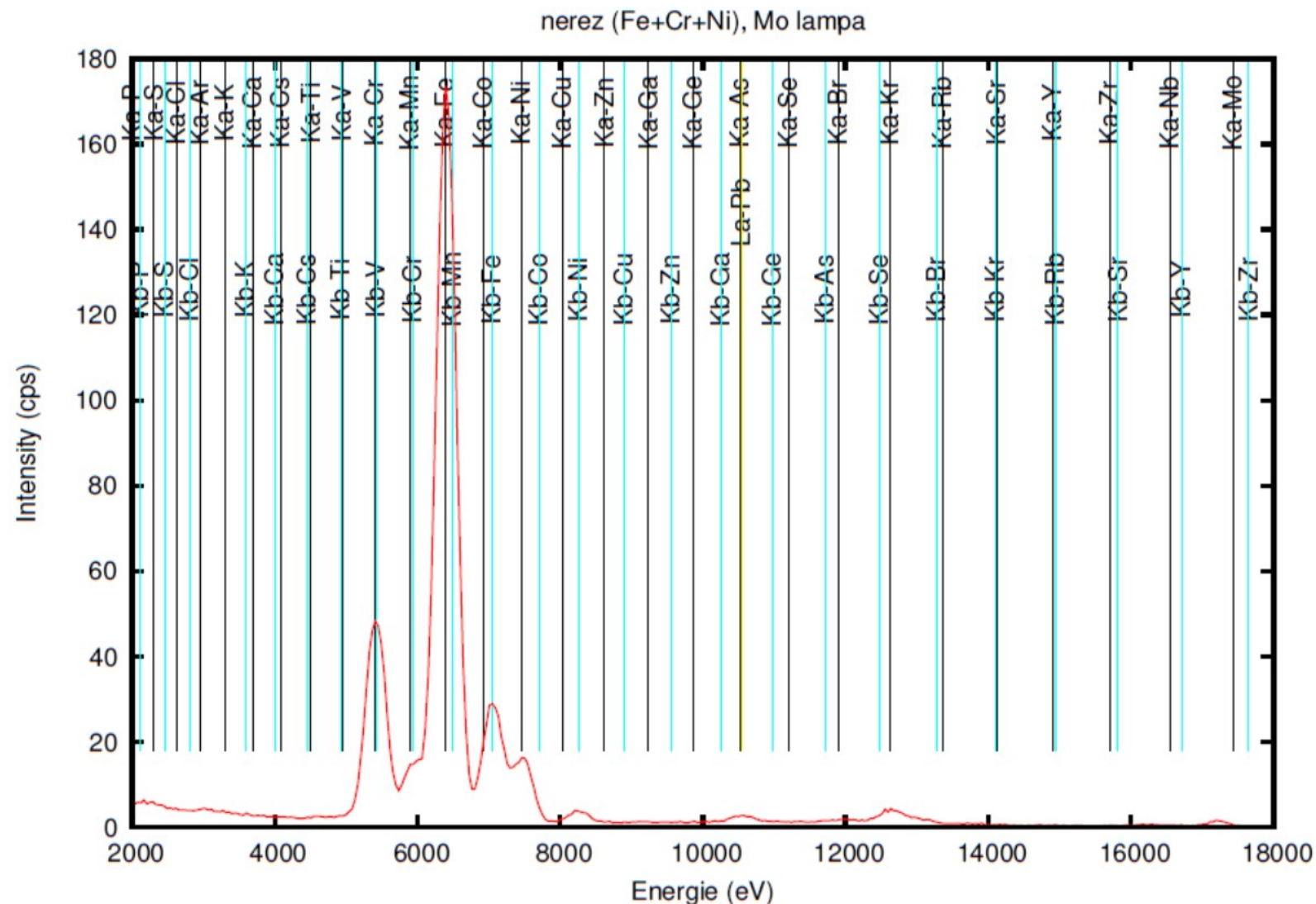
XRF

Rentgenová fluorescenční spektroskopie

X-ray Fluorescence spectroscopy – XRF

Ionizace atomů vzorku rtg svazkem a měření spektra

sekundárního rtg záření. Nezávisí na chemickém stavu atomu.

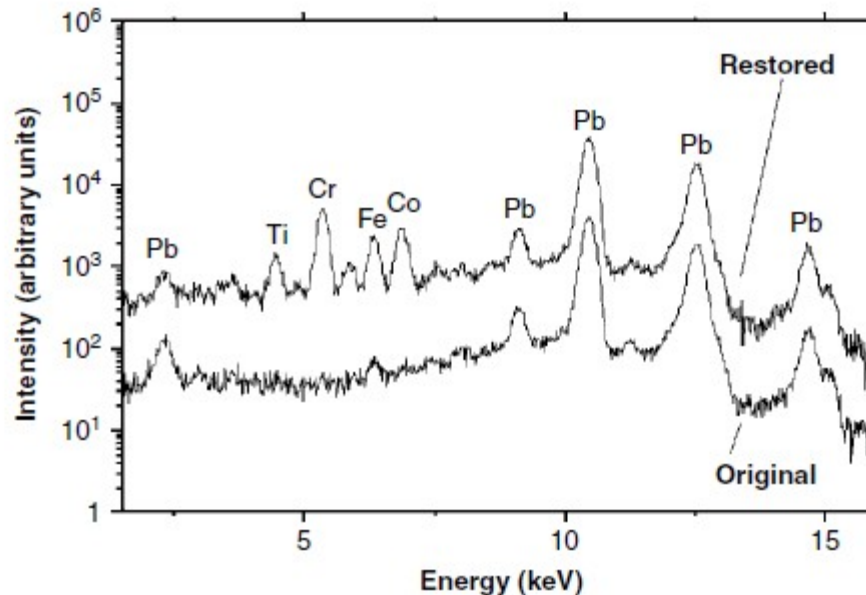


XRF

Rentgenová fluorescenční spektroskopie Kvantitativní analýza:



(a)



(b)

Figure 3.3.15 (a) Micro-XRF analysis of a baroque painting (attributed to P. Thys). The area marked '1' shows Fe, Pb but no Co or Cu, suggesting the use of indigo (an organic pigment), the area marked '2' contains Fe, Hg, Sr, Pb (vermillion), area '3' Ca, Mn, Zn, Pb (umber), and area '4' contains Ca, Mn, Fe, Zn, Pb (umber). (b) Two XRF spectra from adjacent spots in the area marked '1' in (a). Positions where more recent paint (containing Ti, Cr and Co) was applied during past restoration activities can clearly be distinguished from positions with original seventeenth century paint

XRF

Rentgenová fluorescenční spektroskopie
Kvantitativní analýza s použitím j standardů podobného složení,
zanedbány rozdíly absorpce mezi vzorek a standardem:

$$I_i = k_i W_i \quad \text{weight fraction of analyte } W_i$$

$$k_i = \frac{n \sum_{j=1}^n W_{ij} I_{ij} - \sum_{i=1}^n W_{ij} \sum_{i=1}^n I_{ij}}{n \sum_{i=1}^n W_{ij}^2 - \left(\sum_{i=1}^n W_{ij} \right)^2}$$

XRF

Rentgenová fluorescenční spektroskopie
Kvantitativní analýza obecně:

$$I_i = \frac{d\Omega}{4\pi \sin \phi_1} Q_i q_i W_i \int_{\lambda_{\min}}^{\lambda_{edge}} \tau_i(\lambda) I_0(\lambda) \frac{1 - \exp[-\chi(\lambda, \lambda_i) \rho t]}{\chi(\lambda, \lambda_i)} \left(1 + \sum_j W_j S_{ij} \right) d\lambda$$

$d\Omega$ is the differential solid angle for the characteristic radiation

Q_i is the sensitivity of the spectrometer

λ_{min} and λ_{edge} are short-wavelength limit and wavelength of analyte absorption edge,
 $\tau_i(\lambda)$ is the photoelectric absorption coefficient for analyte i

$I_0(\lambda)$ is intensity of the primary radiation

q_i is sensitivity of the analyte i

$q_i = \omega_{K,i} f_{i,K} (1 - 1/J_{i,K})$, where $\omega_{K,i}$ is fluorescence yield of K radiation;
 $J_{i,K}$ is absorption edge jump ratio

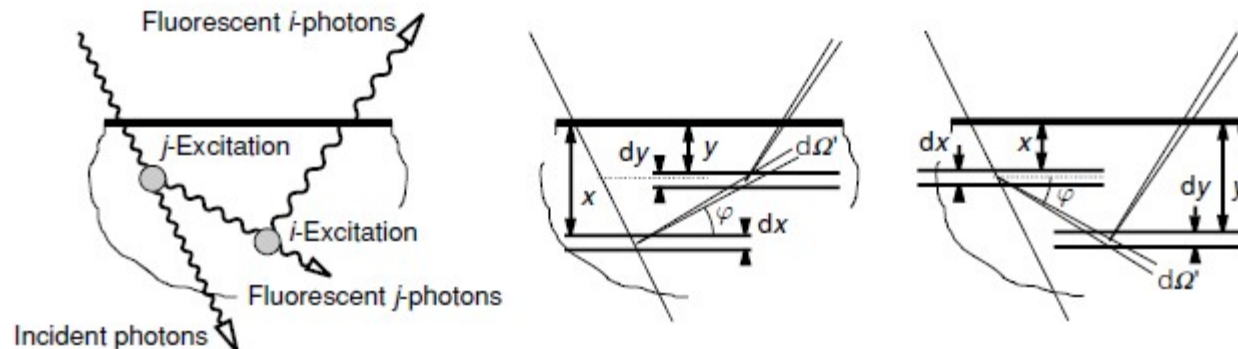
$\chi(\lambda, \lambda_i)$ is total mass-attenuation coefficient of the sample

$$\chi(\lambda, \lambda_i) = \frac{\mu(\lambda)}{\sin \phi_1} + \frac{\mu(\lambda_i)}{\sin \phi_2} \quad \mu(\lambda) = W_i \mu_i(\lambda) + \sum_j W_j \mu_j(\lambda)$$

$$\mu(\lambda_i) = W_i \mu_i(\lambda_i) + \sum_j W_j \mu_j(\lambda_i)$$

XRF

Rentgenová fluorescenční spektroskopie
Kvantitativní analýza efekty self-absorpce:



$$S_{ij} = \frac{1}{2} q_j \tau_j(\lambda) \frac{\tau_i(\lambda_j)}{\tau_i(\lambda)} \frac{\chi(\lambda, \lambda_i)}{1 - \exp[-\chi(\lambda, \lambda_i)\rho t]} D_{ij}$$

$$D_{ij} = \int_0^{\pi/2} \tan(\theta) \left[\frac{1 - \exp[-\chi_1(\lambda_i, \lambda_j)\rho t]}{\chi_1(\lambda_i, \lambda_j)\chi_2(\lambda, \lambda_j)} - \frac{1 - \exp[-\chi(\lambda, \lambda_i)\rho t]}{\chi(\lambda, \lambda_i)\chi_2(\lambda, \lambda_j)} \right] d\theta + \\ \int_{\pi/2}^{\pi} \tan(\theta) \left[\frac{\exp[-\chi_2(\lambda, \lambda_j)\rho t] - \exp[-\chi(\lambda, \lambda_i)\rho t]}{\chi_1(\lambda_i, \lambda_j)\chi_2(\lambda, \lambda_j)} - \frac{1 - \exp[-\chi(\lambda, \lambda_i)\rho t]}{\chi(\lambda, \lambda_i)\chi_2(\lambda, \lambda_j)} \right] d\theta$$

$$\chi_1(\lambda_i, \lambda_j) = \frac{\mu(\lambda_i)}{\sin \varphi_1} + \frac{\mu(\lambda_j)}{\cos \theta}$$

$$\chi_2(\lambda, \lambda_j) = \frac{\mu(\lambda)}{\sin \varphi_1} - \frac{\mu(\lambda_j)}{\cos \theta}$$

XRF

Rentgenová fluorescenční spektroskopie
Kvantitativní analýza limita pro tlustý vzorek:

$$I_i = \frac{d\Omega}{4\pi \sin \phi} Q_i q_i W_i \int_{\lambda_{\min}}^{\lambda_{edge}} \frac{\tau_i(\lambda) I_0(\lambda)}{\chi(\lambda, \lambda_i)} \left(1 + \sum_j W_j S_{ij} \right) d\lambda$$

$$S_{ij} = \frac{1}{2} q_j \tau_j(\lambda) \frac{\tau_i(\lambda_j)}{\tau_i(\lambda)} \left[\ln \left(1 + \frac{\mu(\lambda)}{\mu(\lambda_j) \sin \phi_1} \right) \frac{\sin \phi_1}{\mu(\lambda)} + \ln \left(1 + \frac{\mu(\lambda_i)}{\mu(\lambda_j) \sin \phi_2} \right) \frac{\sin \phi_2}{\mu(\lambda_i)} \right]$$

$$t \geq \frac{4.61}{\chi(\lambda, \lambda_i) \rho}$$

Limita pro tenký vzorek:

$$I_i = \frac{d\Omega}{4\pi \sin \phi} Q_i q_i W_i \rho t \int_{\lambda_{\min}}^{\lambda_{edge}} \tau_i(\lambda) I_0(\lambda) d\lambda \quad \rho t \leq \frac{0.1}{\chi(\lambda, \lambda_i)}$$

XRF

Rentgenová fluorescenční spektroskopie

Total reflexion x-ray fluorescence

monochromatický zdroj, malý úhel dopadu, platí limita tenkého vzorku

analýza povrchové kontaminace polovodičů

- The TXRF-measurements were performed at the PTB beamline for undulator radiation at the electron storage ring BESSY II [2].

High surface layer sensitivity under total reflection geometry

- Based on radiometrically calibrated instrumentation and knowledge of relevant instrumental and atomic fundamental parameters

$$\frac{m_i}{F_i} = \frac{-1}{\mu_{\text{tot},i}} \ln \left\{ 1 - \frac{P_i}{P_{0,\text{Wsurf}} T_{i,E_0} Q} \frac{\Omega_{\text{det}}}{4\pi} \frac{1}{\sin \psi_{\text{in}}} \frac{1}{\mu_{\text{tot},i}} \right\}$$

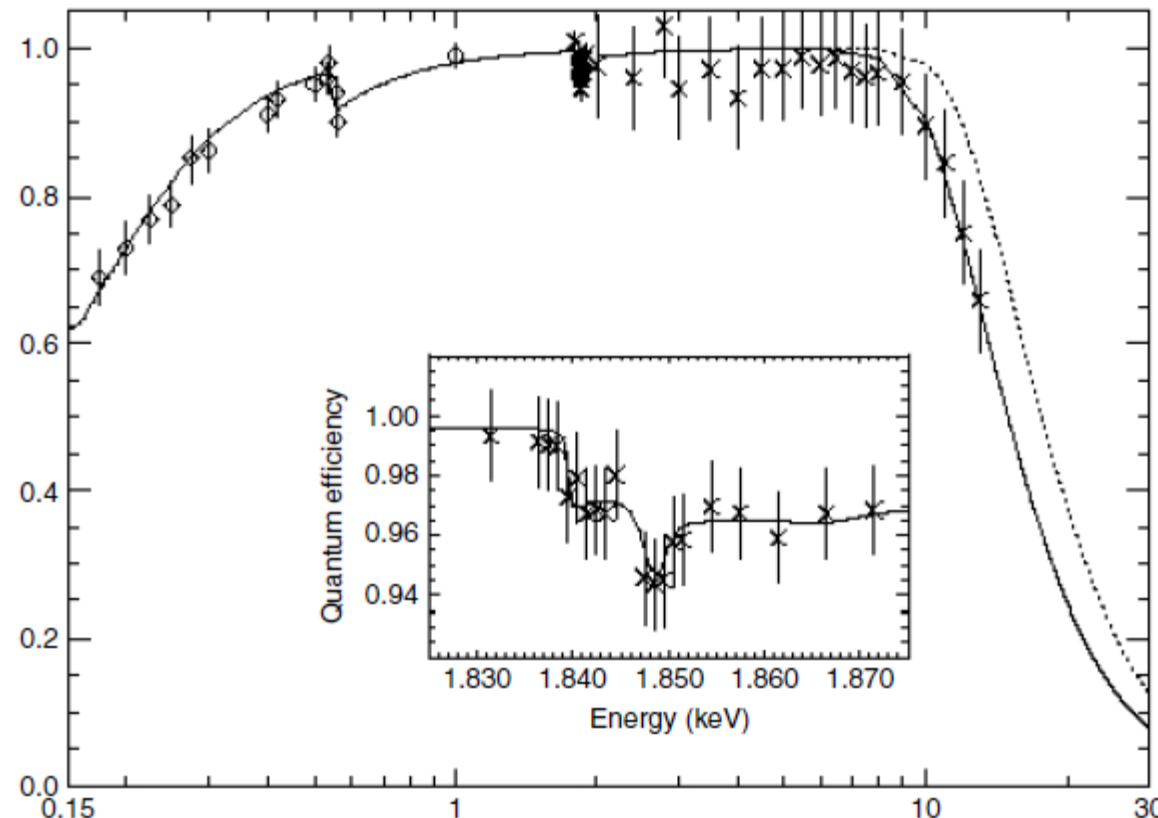
P: radiant power
Ω: solid angle of detection
μ, T, Q: fundamental materials parameters
ψ: Incident Angle of radiation

Mass deposition of the element / can be directly calculated [3]

Surface concentration / Gallane density

XRF

Rentgenová fluorescenční spektroskopie Kvantitativní analýza:



4.1.14 Quantum efficiency for X-rays in the range of 150 eV to 30 keV energy of a pn-CC of 300 μm thickness (open diamonds and solid line) equipped with a thin optimized radiation entrance window. Close to 100 % quantum efficiency held over most of the range. Remarkable is the high efficiency at low energies. The falloff at high energy is due to the thickness. The dotted line represents an extrapolation to 500 μm thick sensitive volume

X-ray standing waves

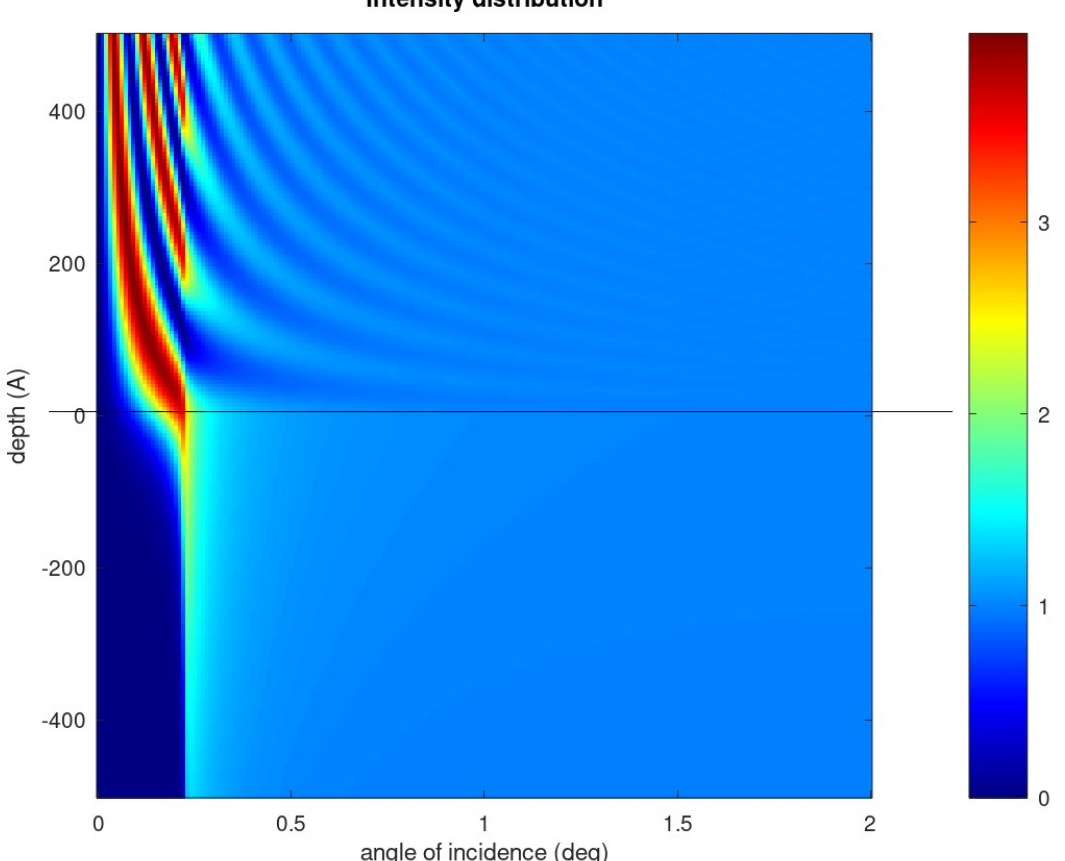
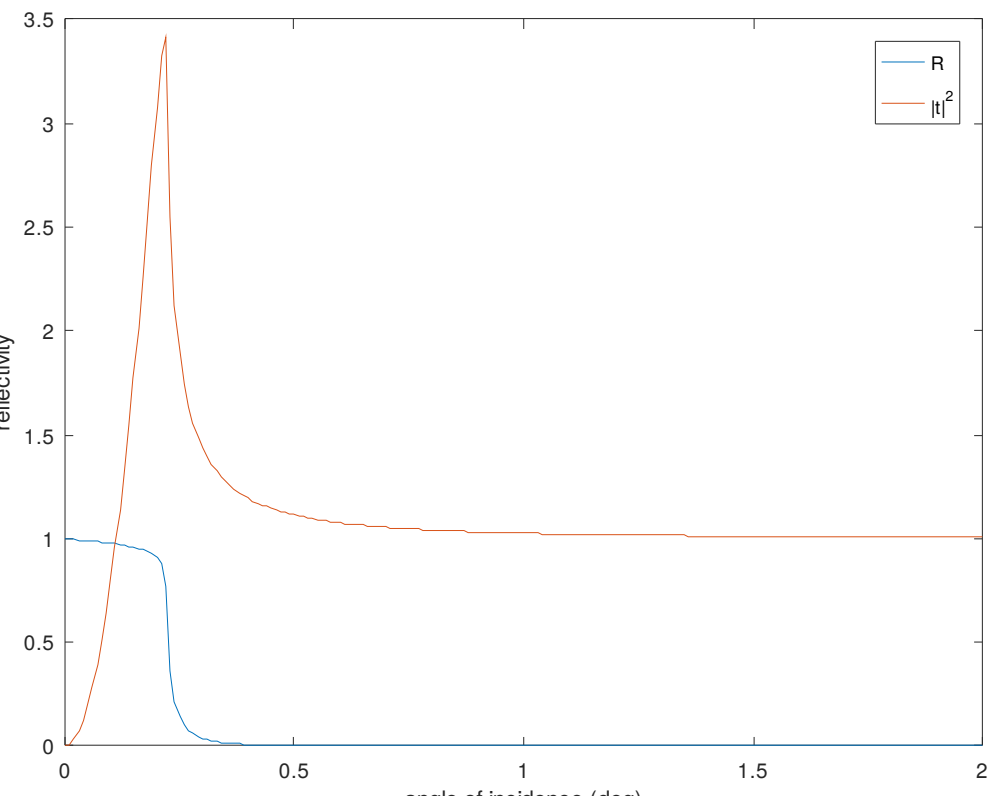
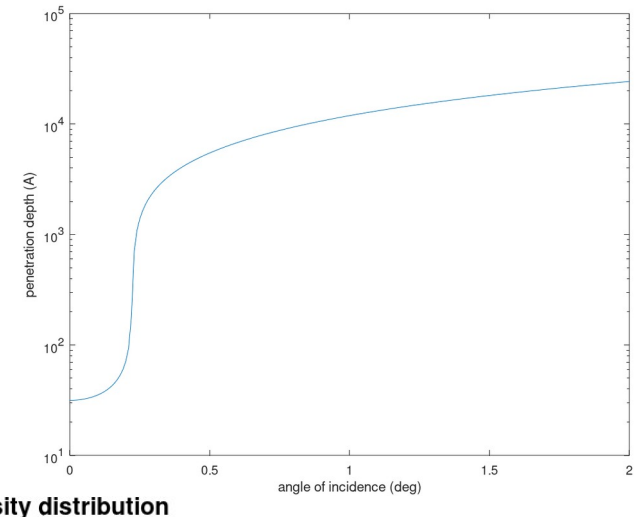
Total x-ray reflection

Above surface

$$\exp(i K_z z) + r \exp(-i K_z z)$$

Below surface

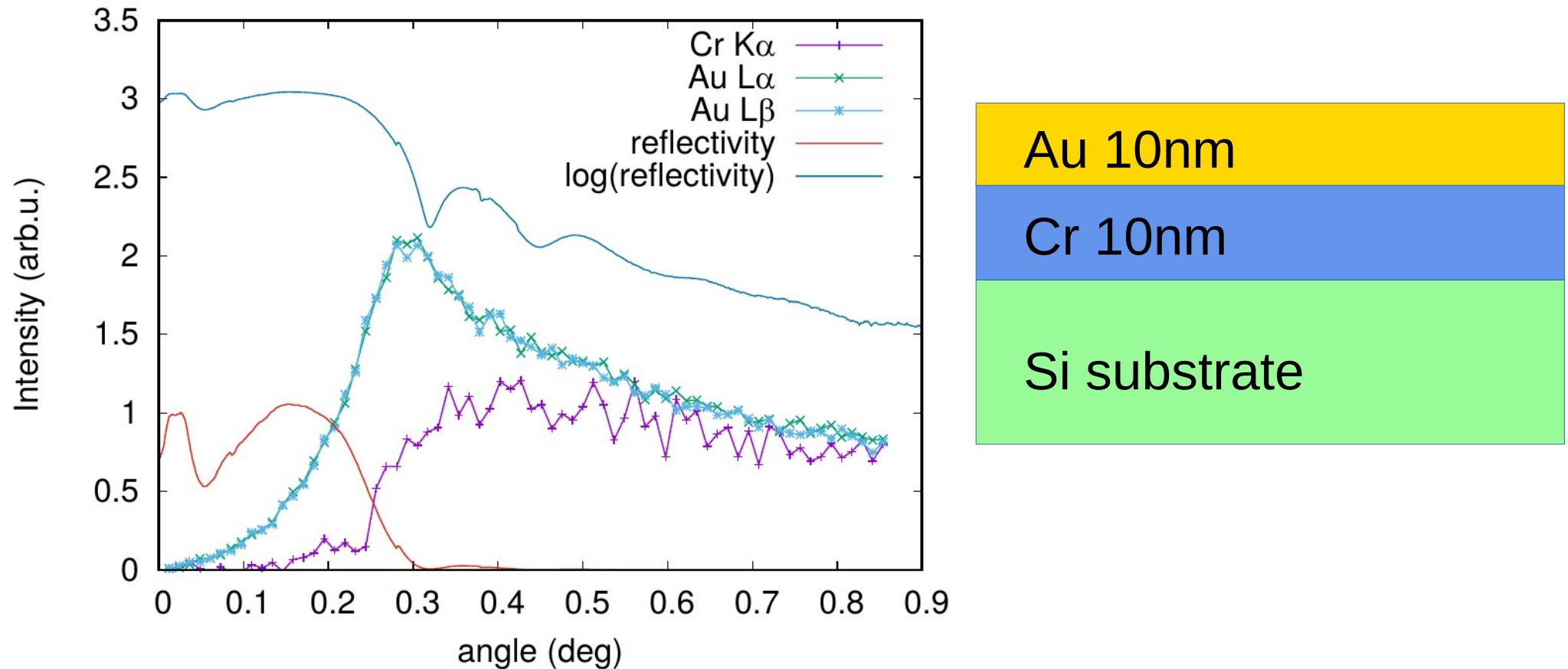
$$t \exp(i k_z z)$$



X-ray standing waves

Total reflection

Testing sample (Csaba Morvay)

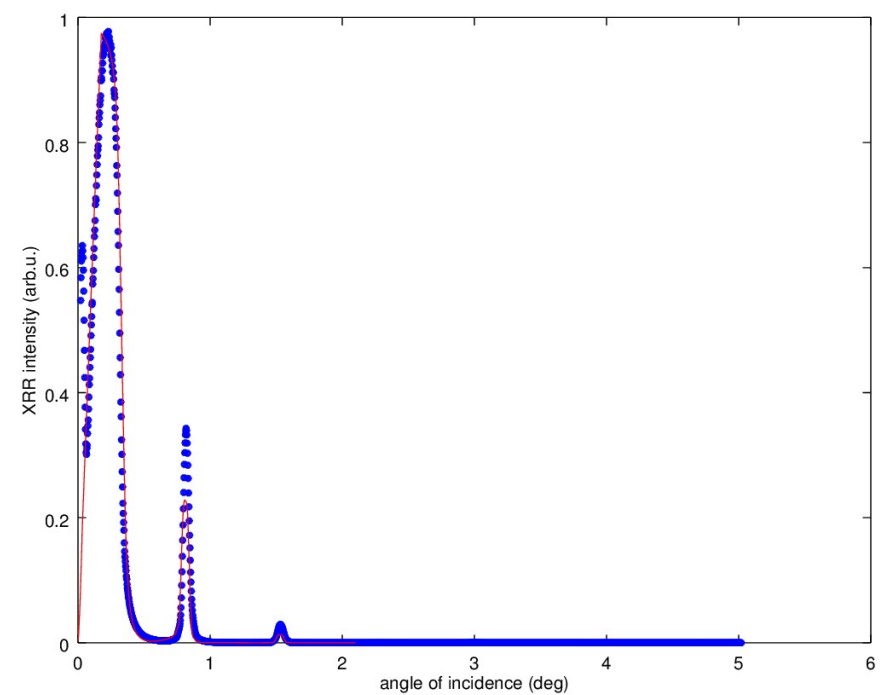
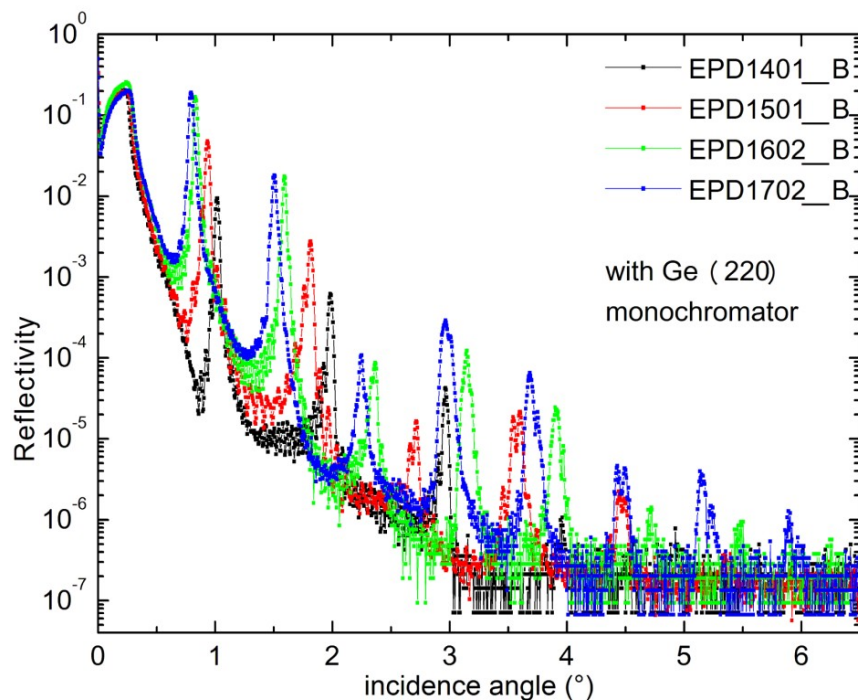


X-ray standing waves

Multilayers

X-ray reflectivity: superlattice peaks

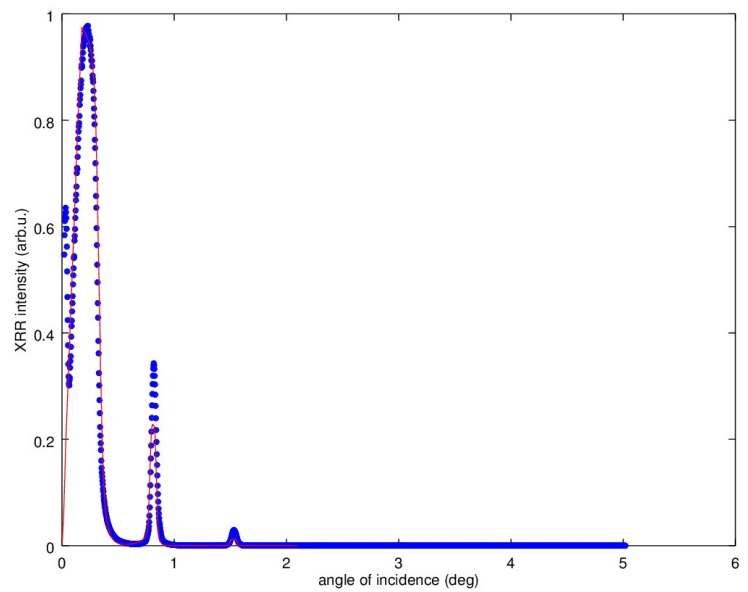
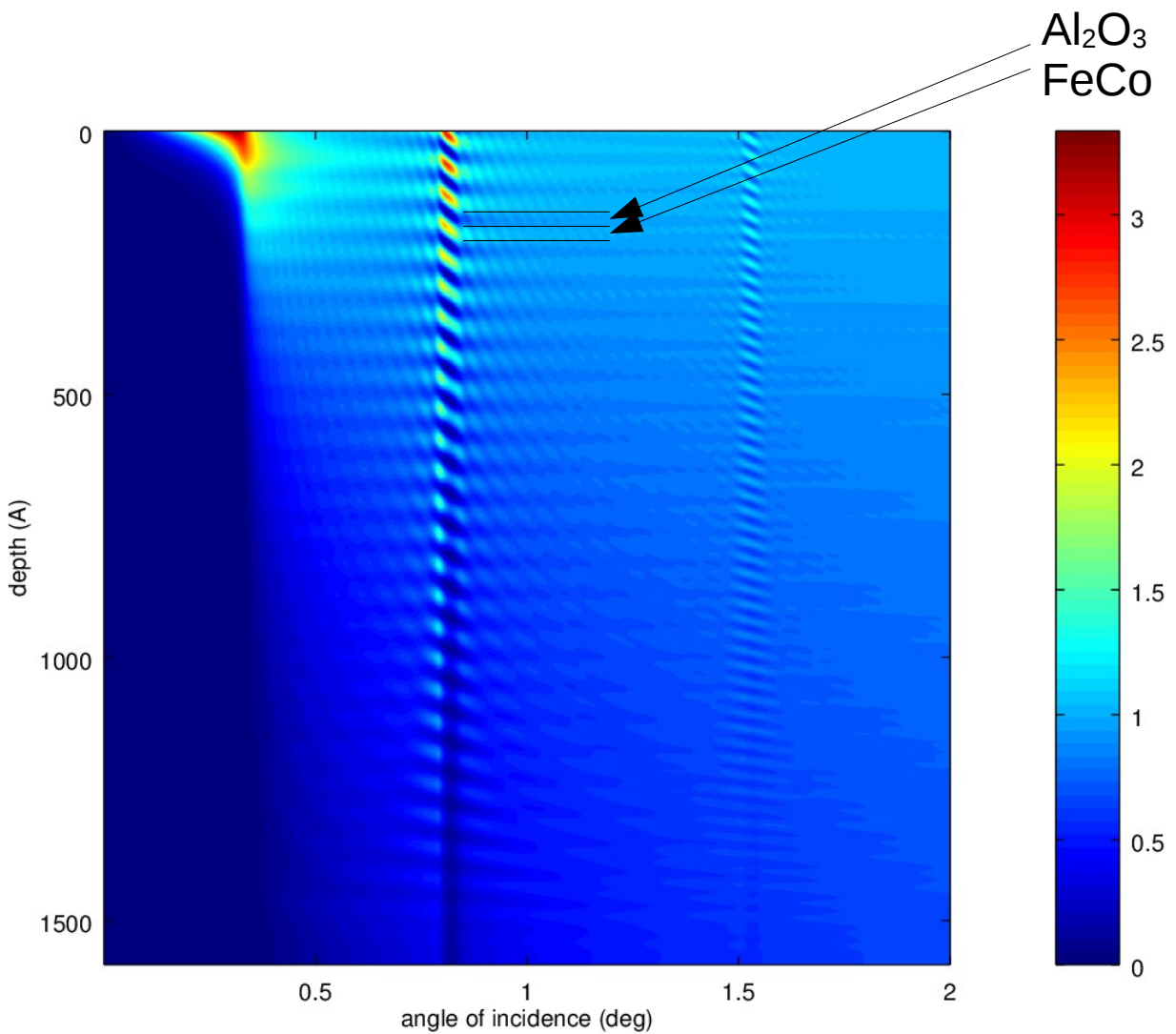
Bragg peaks corresponding superlattice period



X-ray standing waves

Multilayers

Depth Intensity distribution



X-ray standing waves

Samples: superparamagnetic multilayers

EPD layers in Load Lock Sputtering system

25x($\text{Fe}_{60}\text{Co}_{40}/\text{Al}_2\text{O}_3$) multilayers were prepared, with 3.5 nm nominal thick Al_2O_3 interlayers and the nominal layer thickness of the $\text{Fe}_{60}\text{Co}_{40}$ layers was changed from 0.5 nm to 2 nm + (5 nm Al_2O_3 buffer layer)

$\text{Fe}_{60}\text{Co}_{40}$ target \rightarrow DC sputtering (0.5 kW)

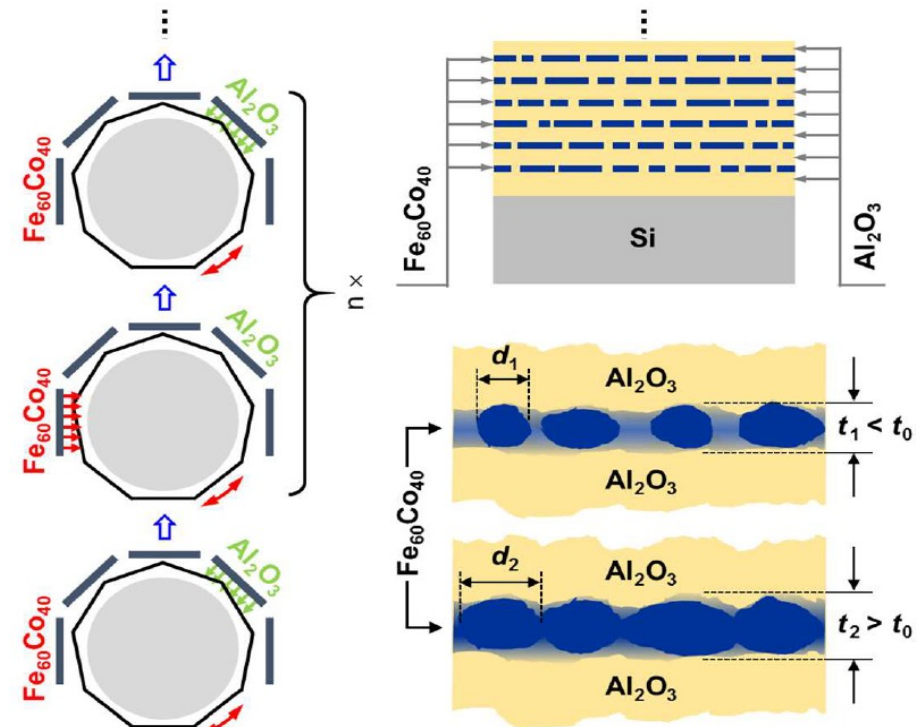
Al_2O_3 standard target \rightarrow RF sputtering (2.5 kW)

multilayers **EPD 14, 15, 16, 17**

$$t_{\text{nominal}} = 0.5, 1.0, 1.5, 2.0 \text{ nm}$$

and another samples **r01-11**
with

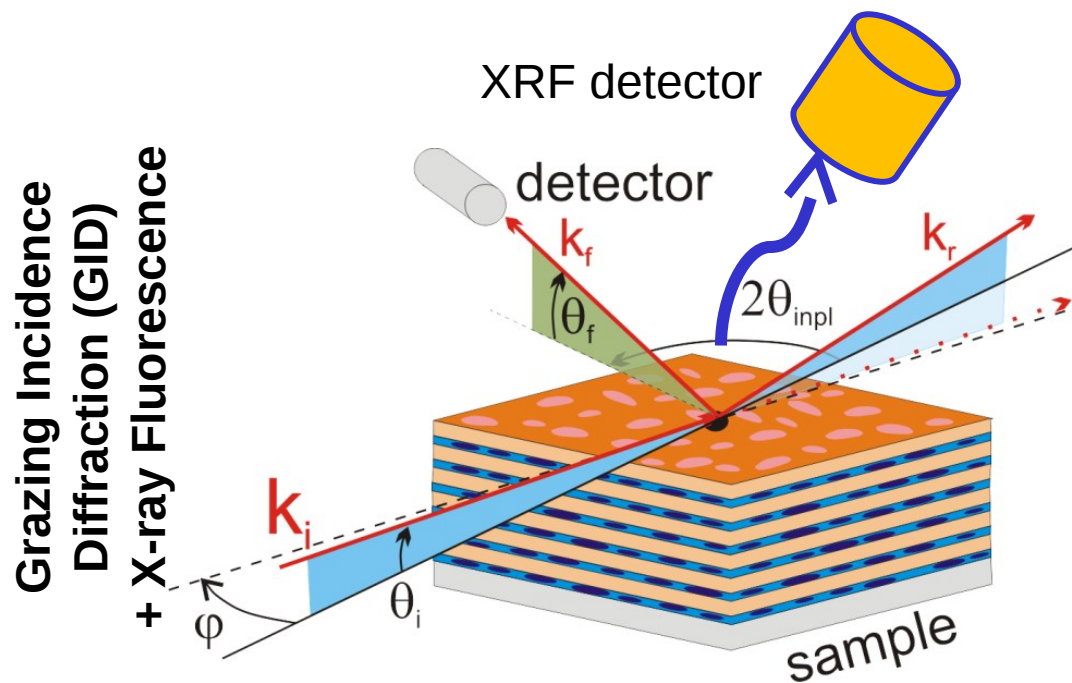
$$t_{\text{nominal}} = 0.5 - 1.5 \text{ nm (0.1 nm step)}$$



X-ray standing waves

Experiment:

- scattering signal FeCo diffraction 002
 - Depth profile of crystalline phase
- Fluorescence signal
 - Chemical depth profile

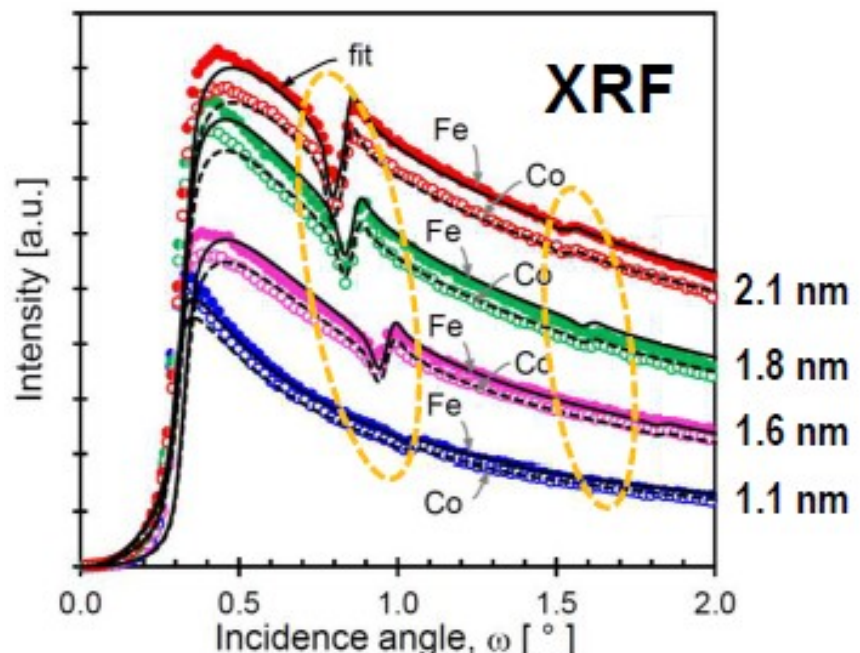
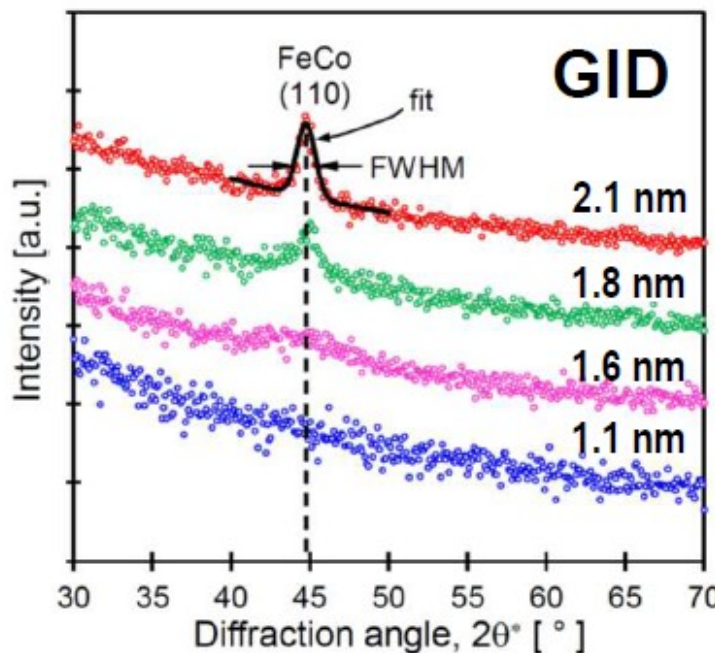
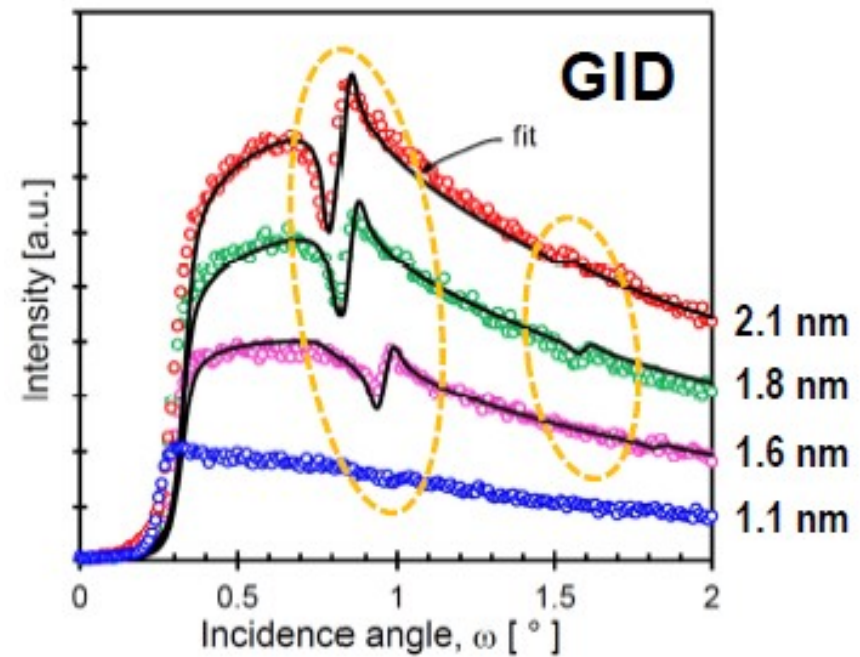


Standing wave x-ray diffraction was studied previously by J. Krčmář (PhD 2009)

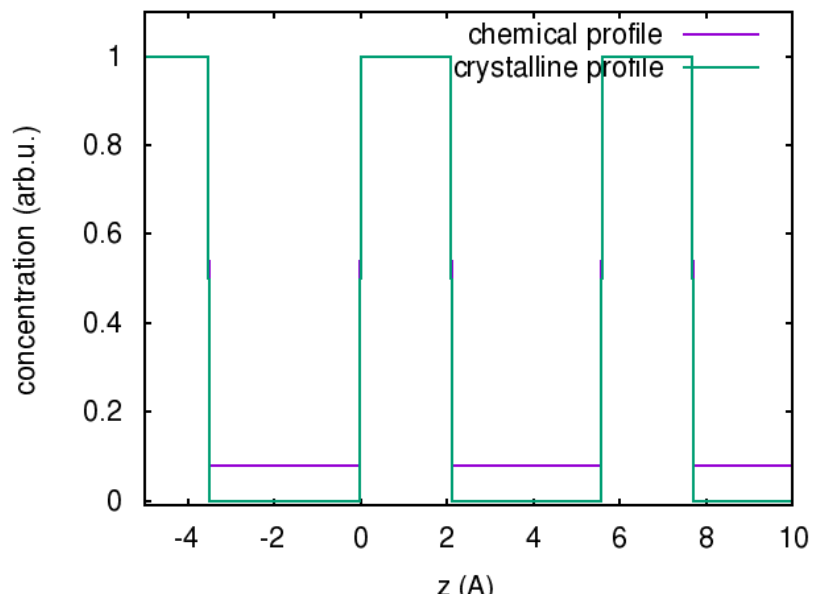
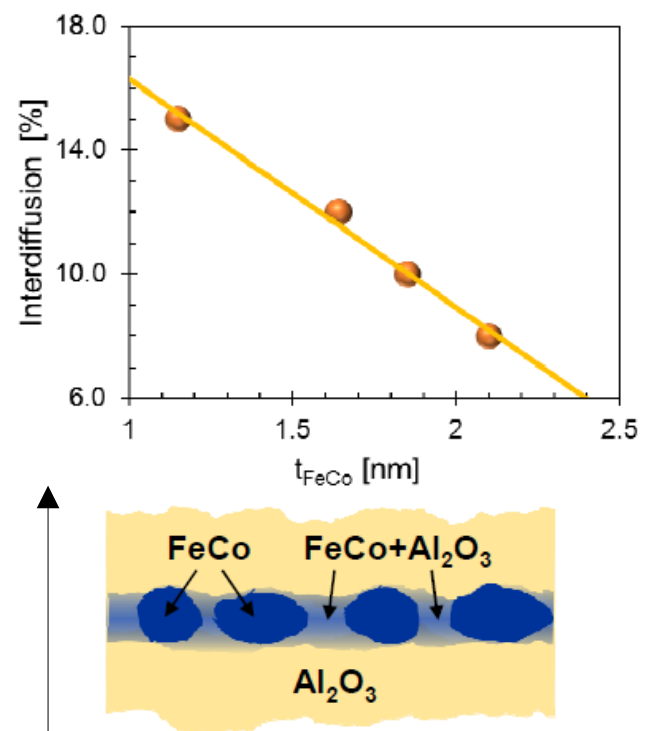
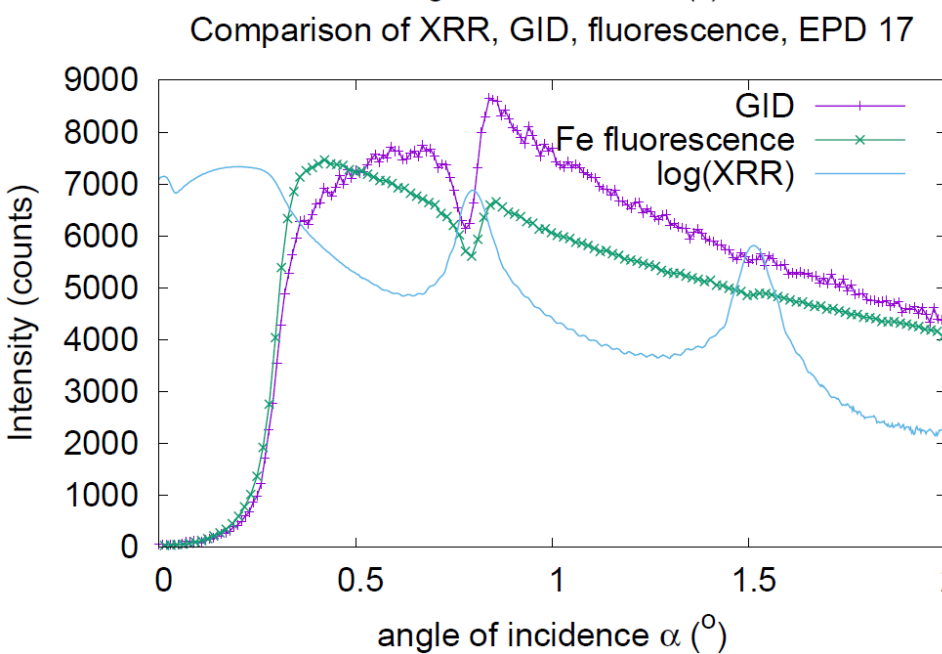
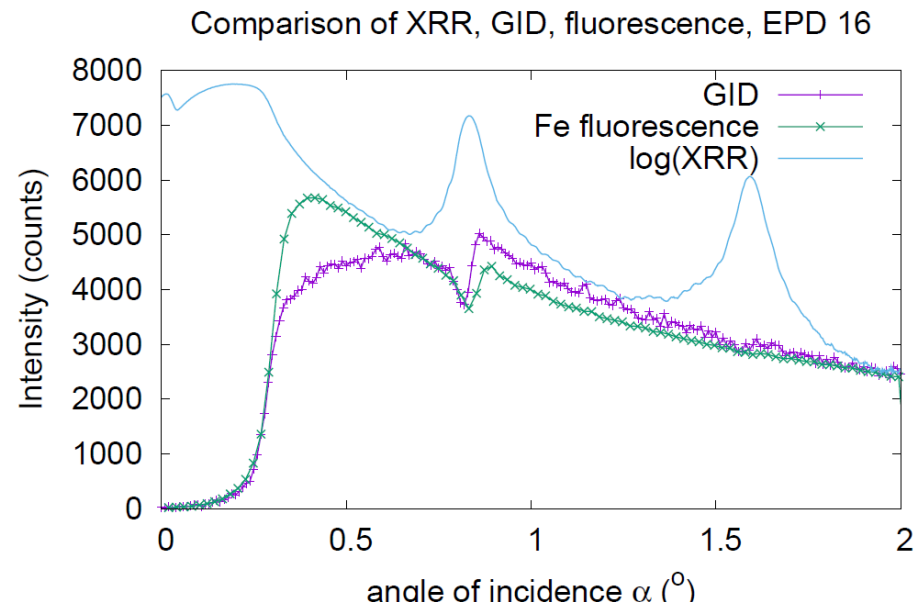
X-ray standing waves

Experiment:

- scattering signal FeCo diffraction 002
 - Depth profile of crystalline phase
- Fluorescence signal



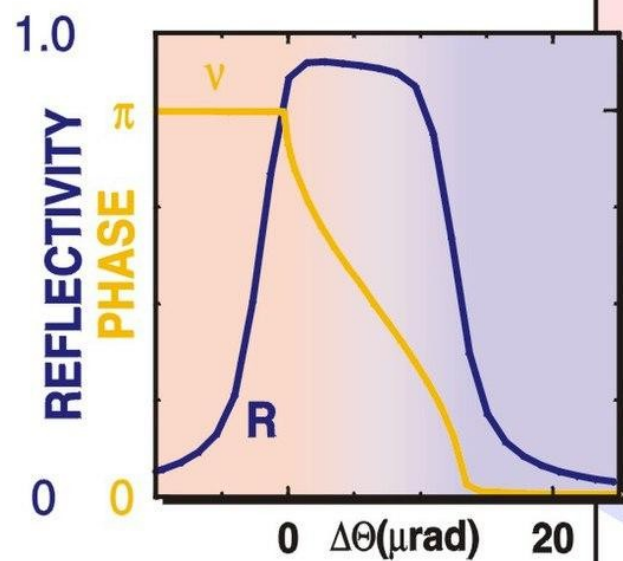
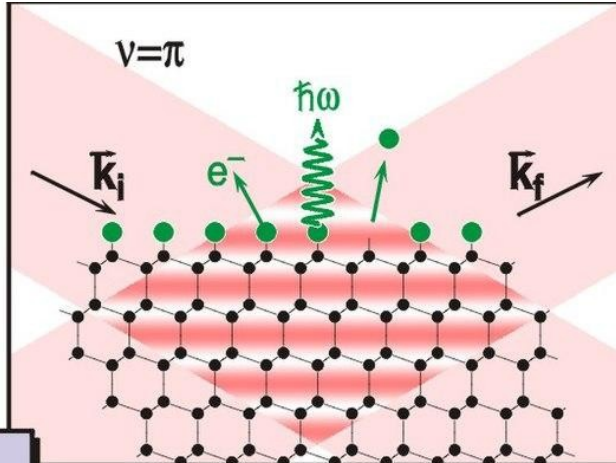
X-ray standing waves



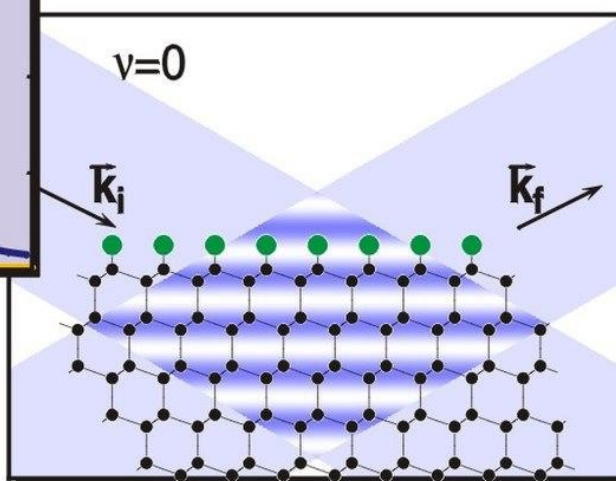
X-ray standing waves

X-ray diffraction

Gerhard Borrmann



- substrate
- adsorbate



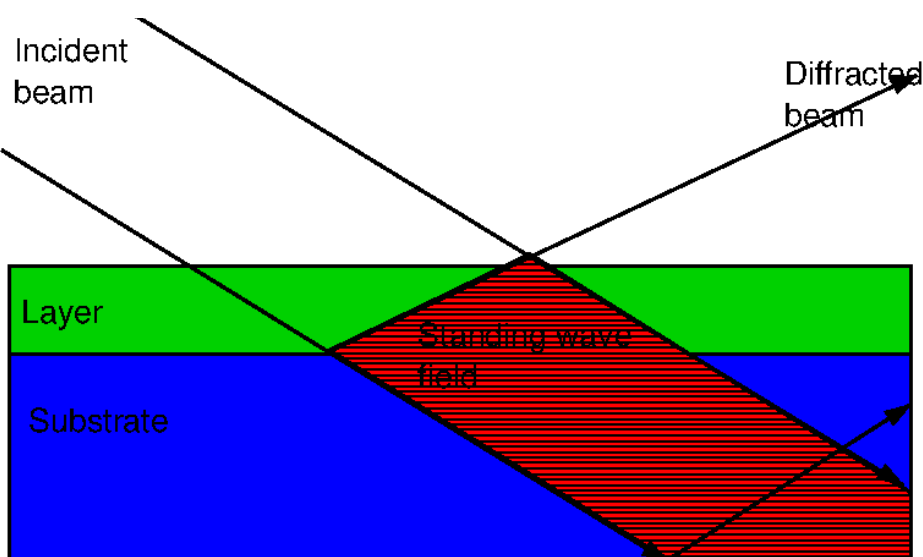
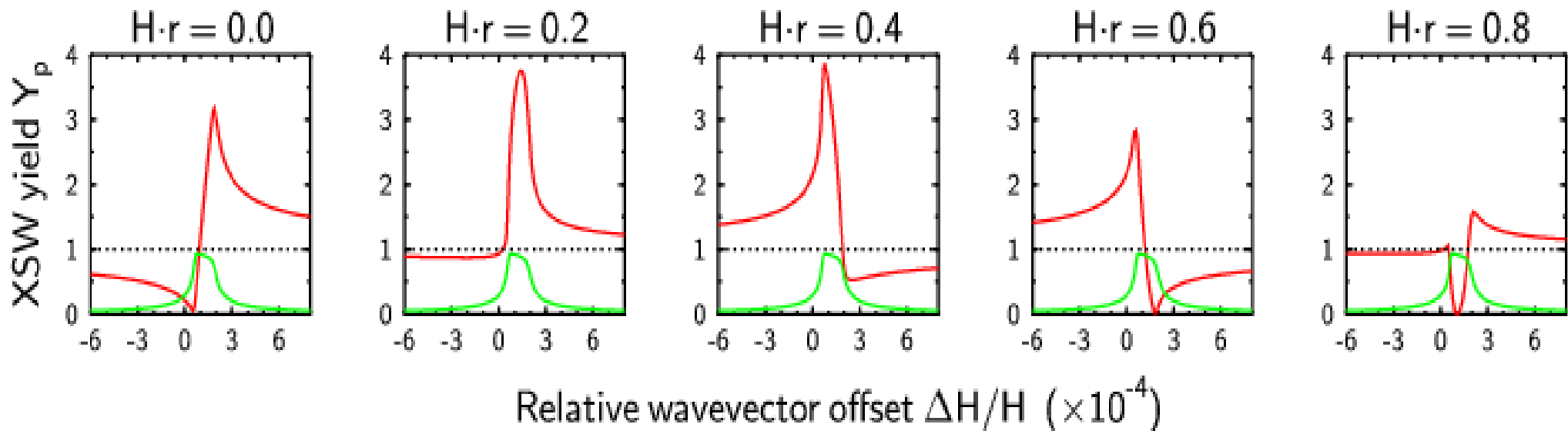
Boris Batterman



X-ray standing waves

X-ray diffraction

$$Y_p(\Omega) = 1 + R + 2C\sqrt{R}f_H \cos(\nu - 2\pi P_H)$$

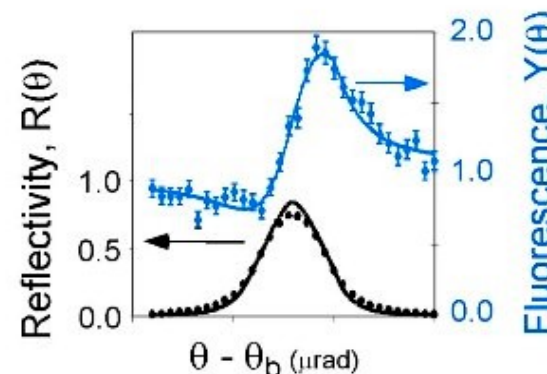
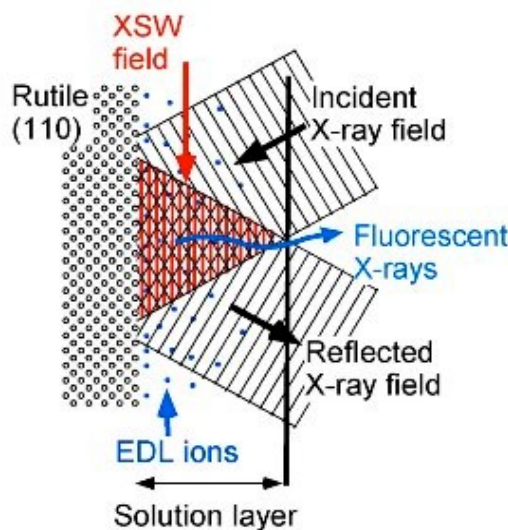
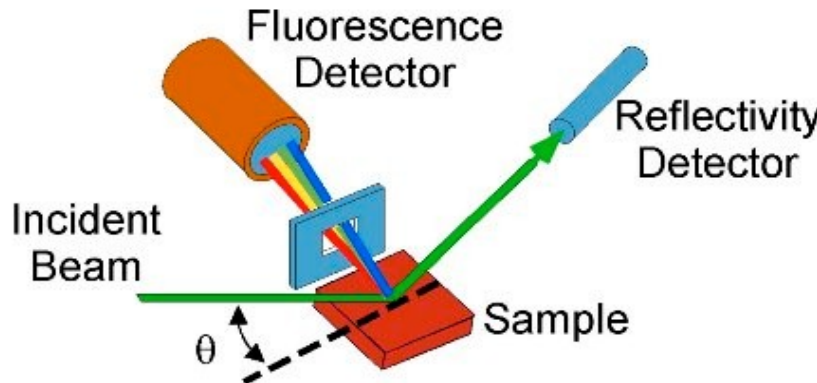


Standing wave in thin film induced by substrate

Period of standing wave defined by monocrystalline substrate:
InP (111) $d=3.39 \text{ \AA}$

Film thickness limited by lattice mismatch!

Fluorescence ve stojaté vlně



Fluorescent yield:

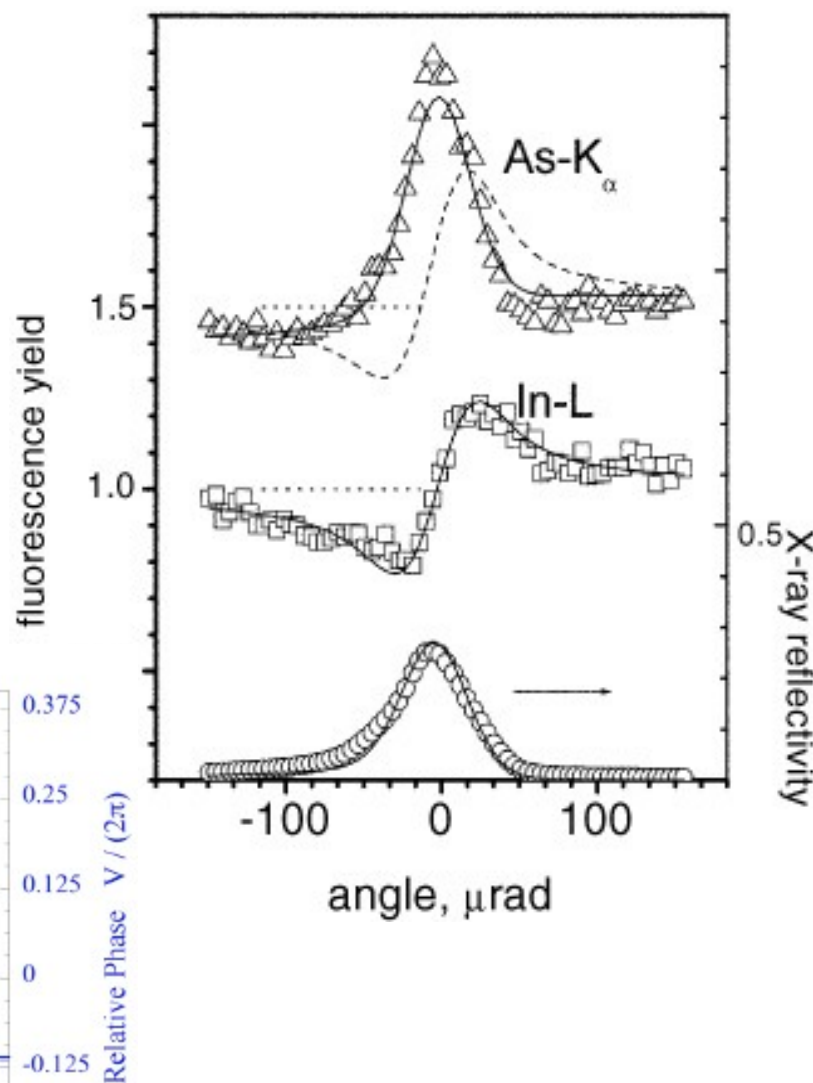
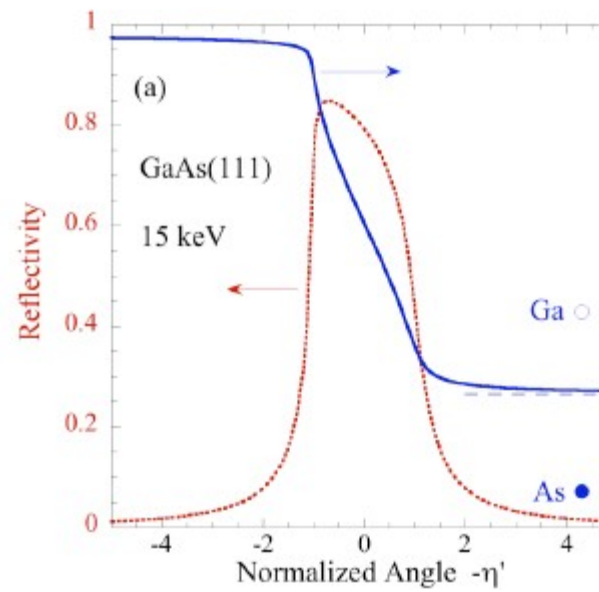
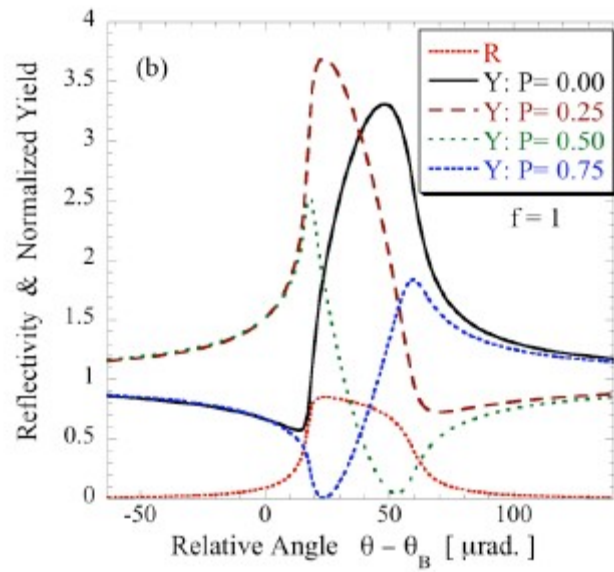
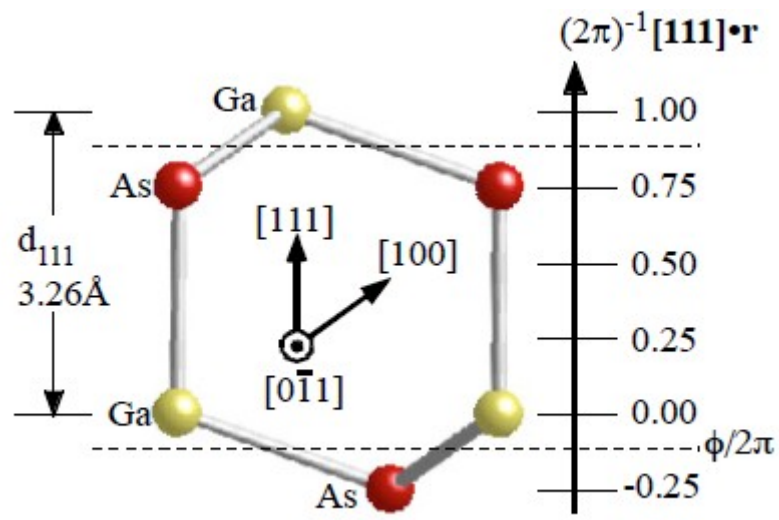
$$Y_H(\theta)/Y_{OB} = 1 + R(\theta) + 2F_H [R(q)]^{1/2} \cos[\nu(\theta) - 2\pi P_H]$$

P_H ("coherent position") and F_H ("coherent fraction") describe the ion distribution. A first-order analysis of these parameters with respect to EDL structure yields:

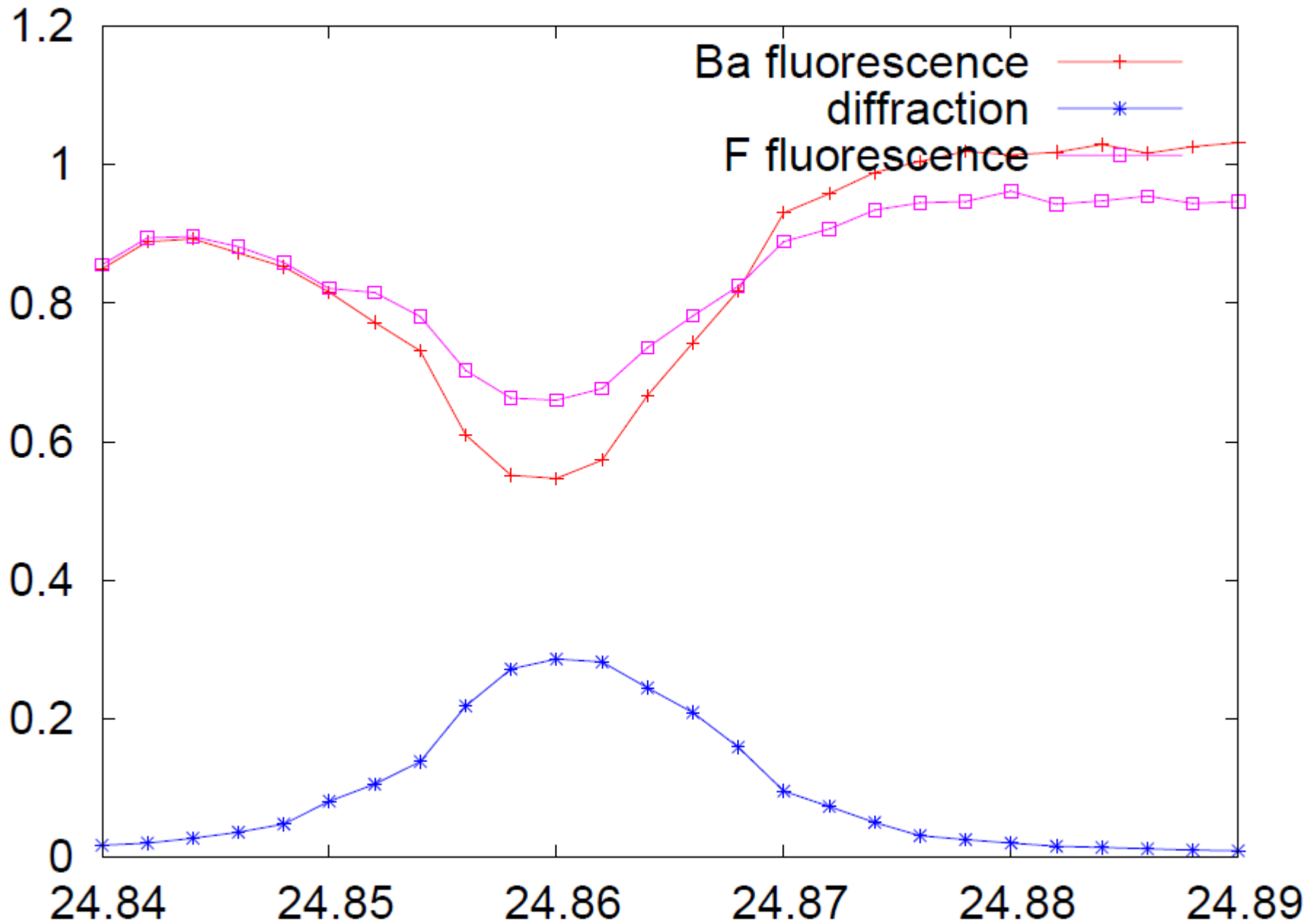
$P \sim h/d_H$, (h is ion height w/r to H^{th} Bragg plane)

$F \sim$ fraction of double layer ions in adsorbed condensed layer

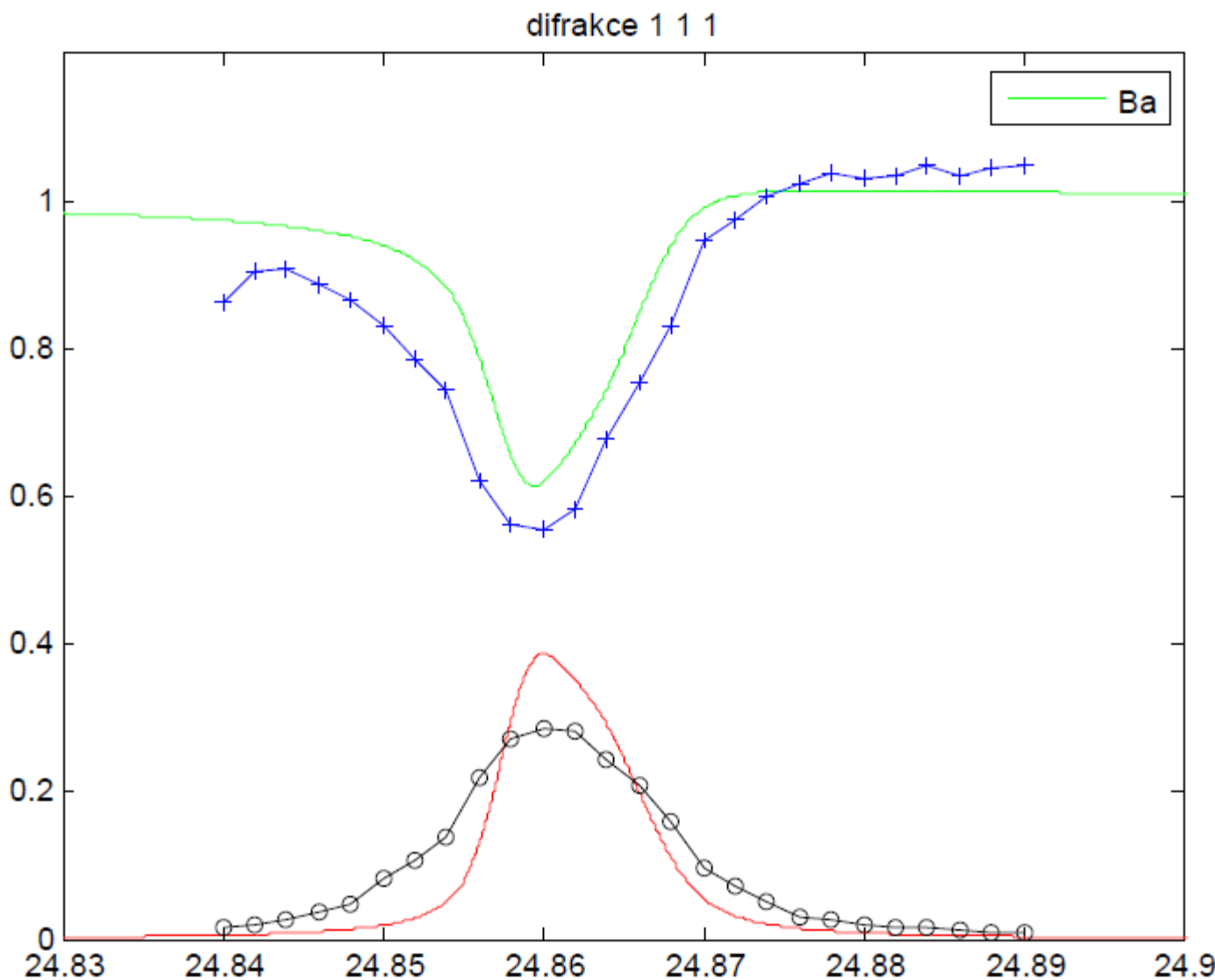
Fluorescence ve stojaté vlně



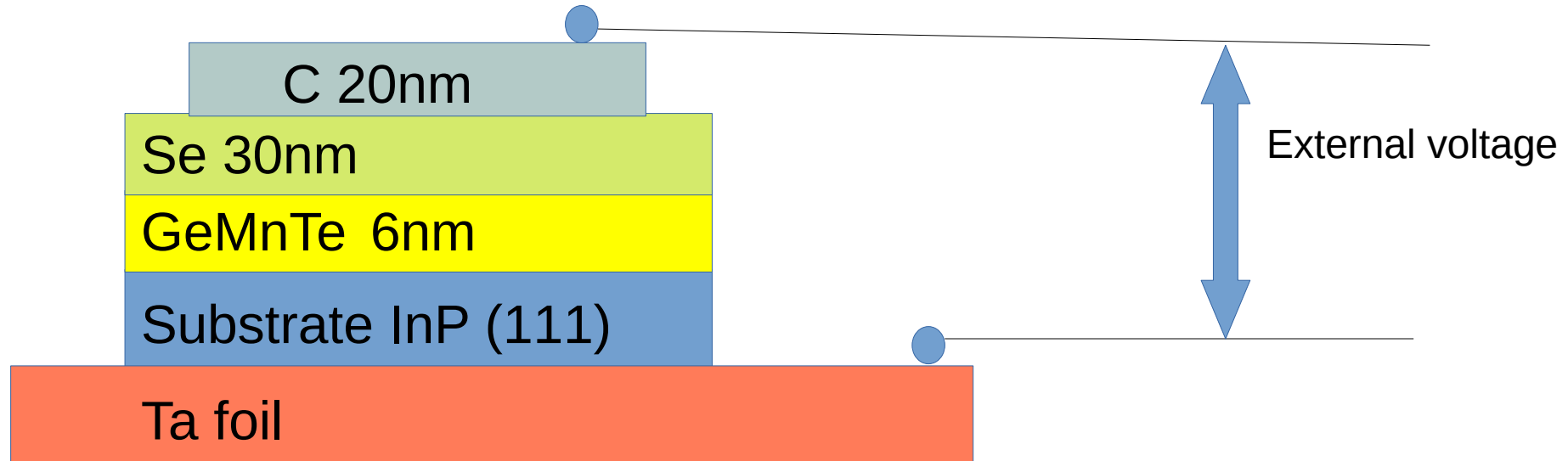
Fluorescence ve stojaté vlně



Fluorescence ve stojaté vlně



Standing waves in (Ge,Mn)Te



Sample preparation:
JKU Linz

VA2268 6nm
GeTe/InP(111)A
+ 30nm Se cap
+ 20nm carbon (one piece)

VA2269 6nm
GeMnTe/InP(111)A
+ 30nm Se cap
+ 20nm carbon (one piece)

VA2270 6nm
GeTe/InP(111)A
+ 30nm Se cap
+ 20nm carbon (one piece)

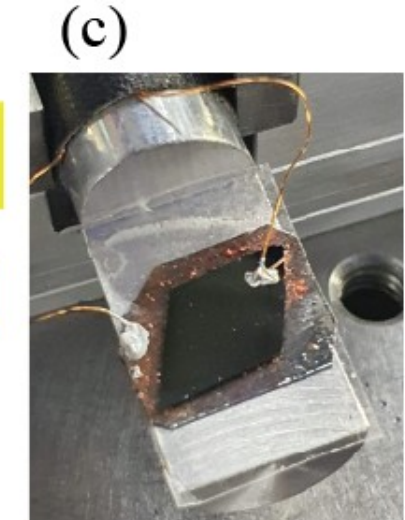
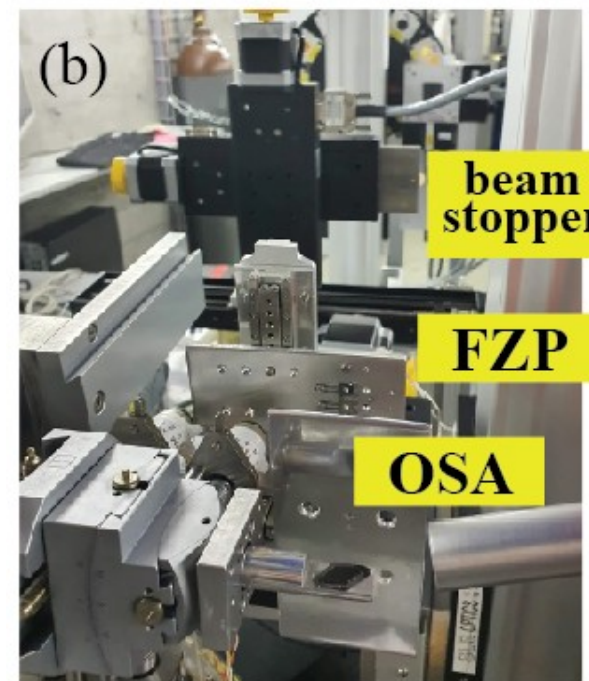
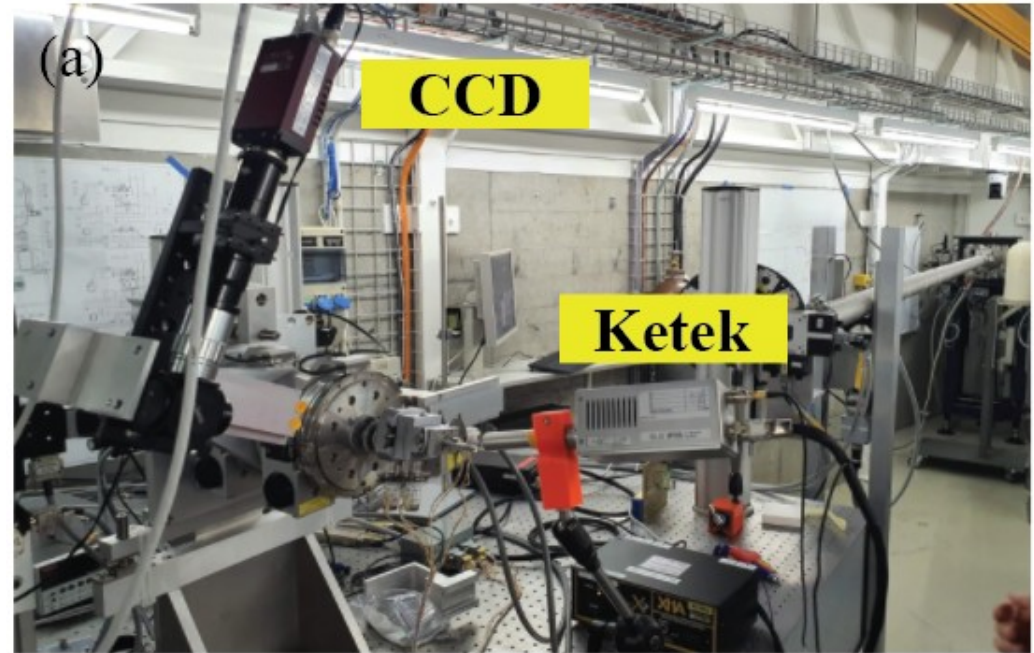


Standing waves in (Ge,Mn)Te

Experiment at synchrotron
swiss light source – SLS

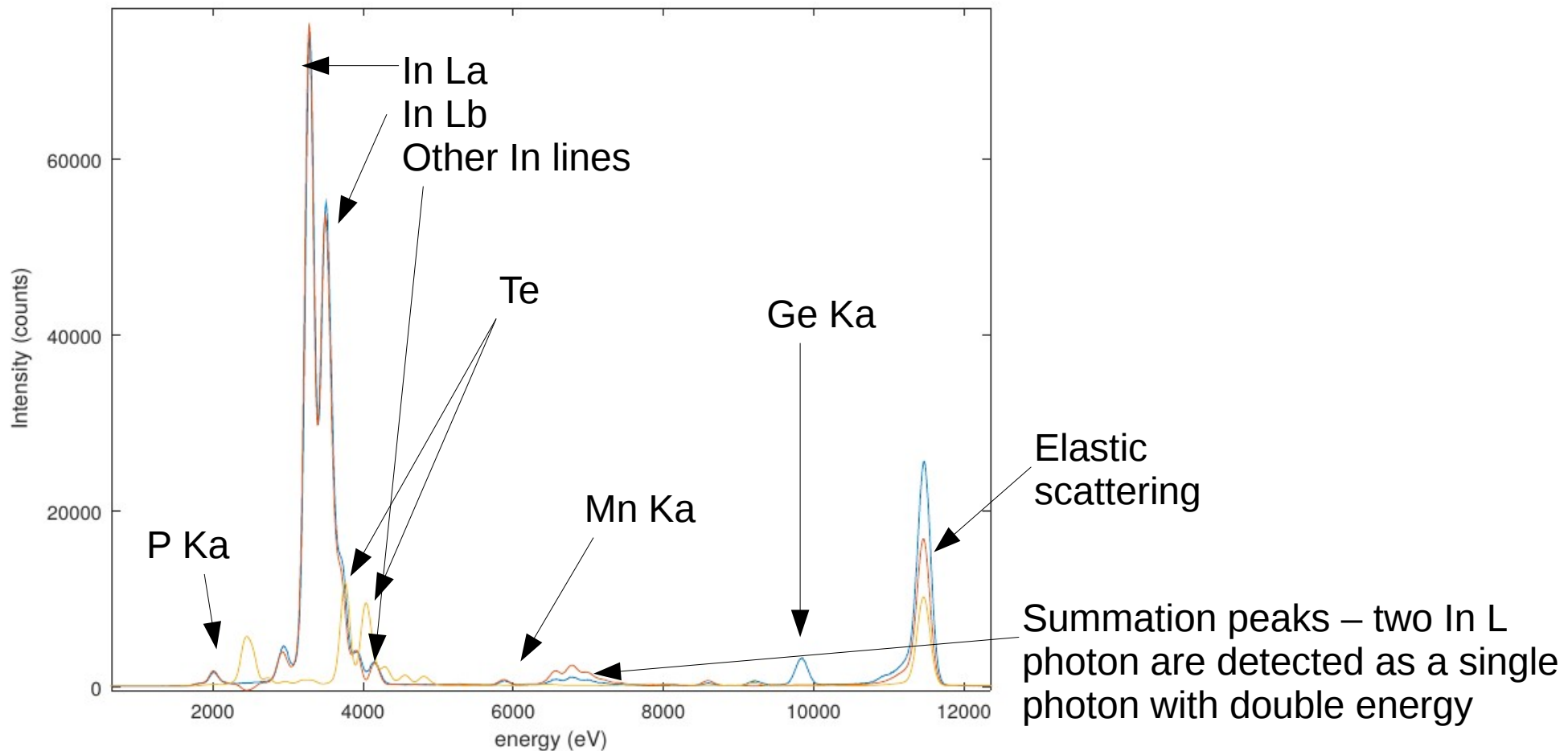
Beamline X05DA

Photon energy 11.5 keV
above Ge K edge
to excite Ge K lines

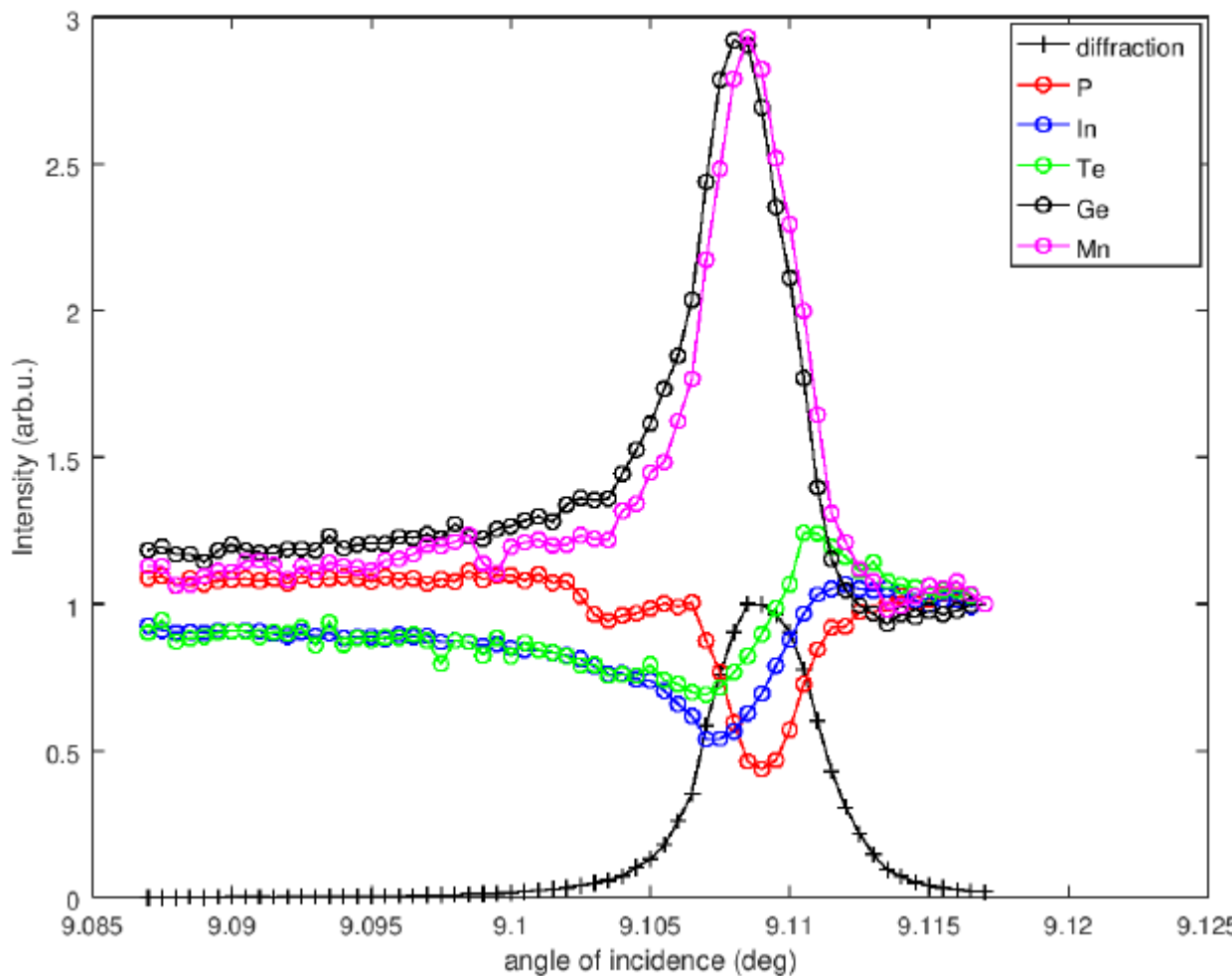


Standing waves in (Ge,Mn)Te

X-ray fluorescence spectrum



Standing waves in (Ge,Mn)Te



Average positions in fraction of standing wave period –
InP (111) interplanar distance 3.39 Å

GeTe and GeMnTe

In: 0.05

P: 0.77

In and P distance confirms
InP (111)A – In terminated
orientation

GeMnTe:

Te: 0.86

Ge: 0.37

Mn: 0.32

Te-Ge planes 1.52 Å

GeTe:

Te: 0.86

Ge: 0.45

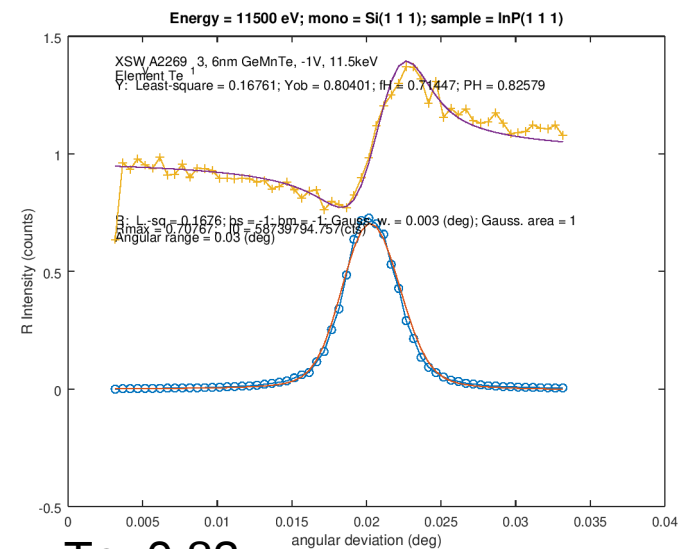
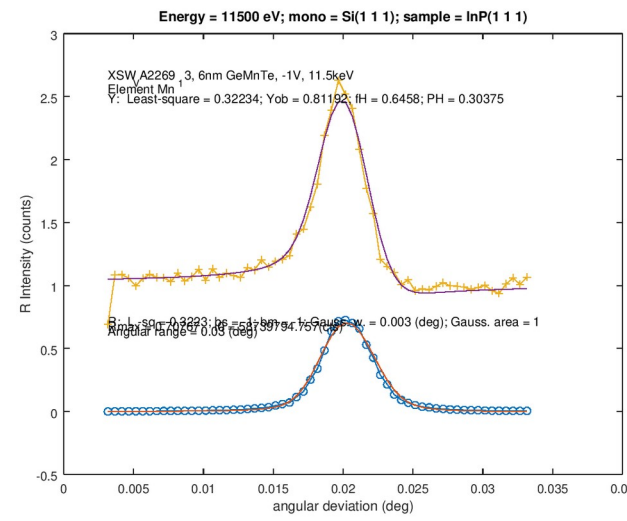
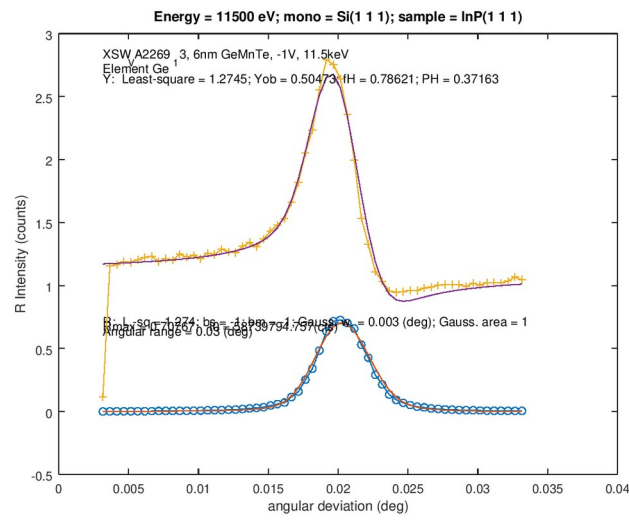
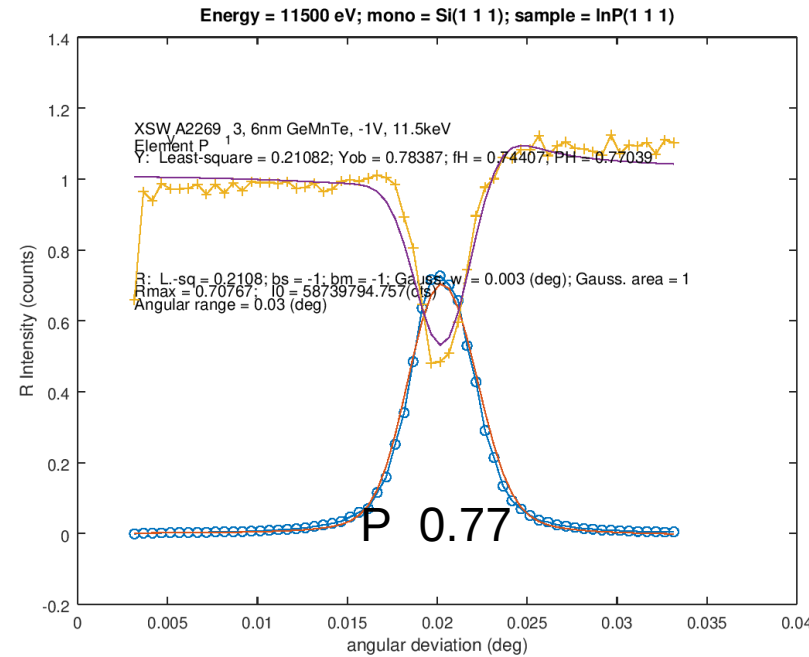
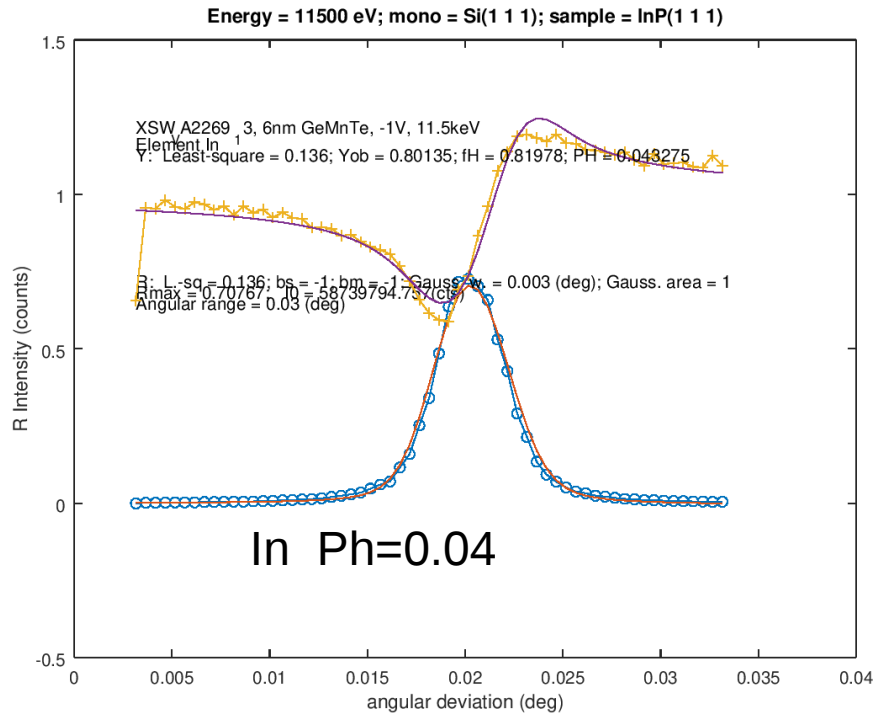
Te-Ge planes 1.40 Å

Distance of Ge-Te planes:
High temperature rocksalt
Ferroelectric rhombohedral

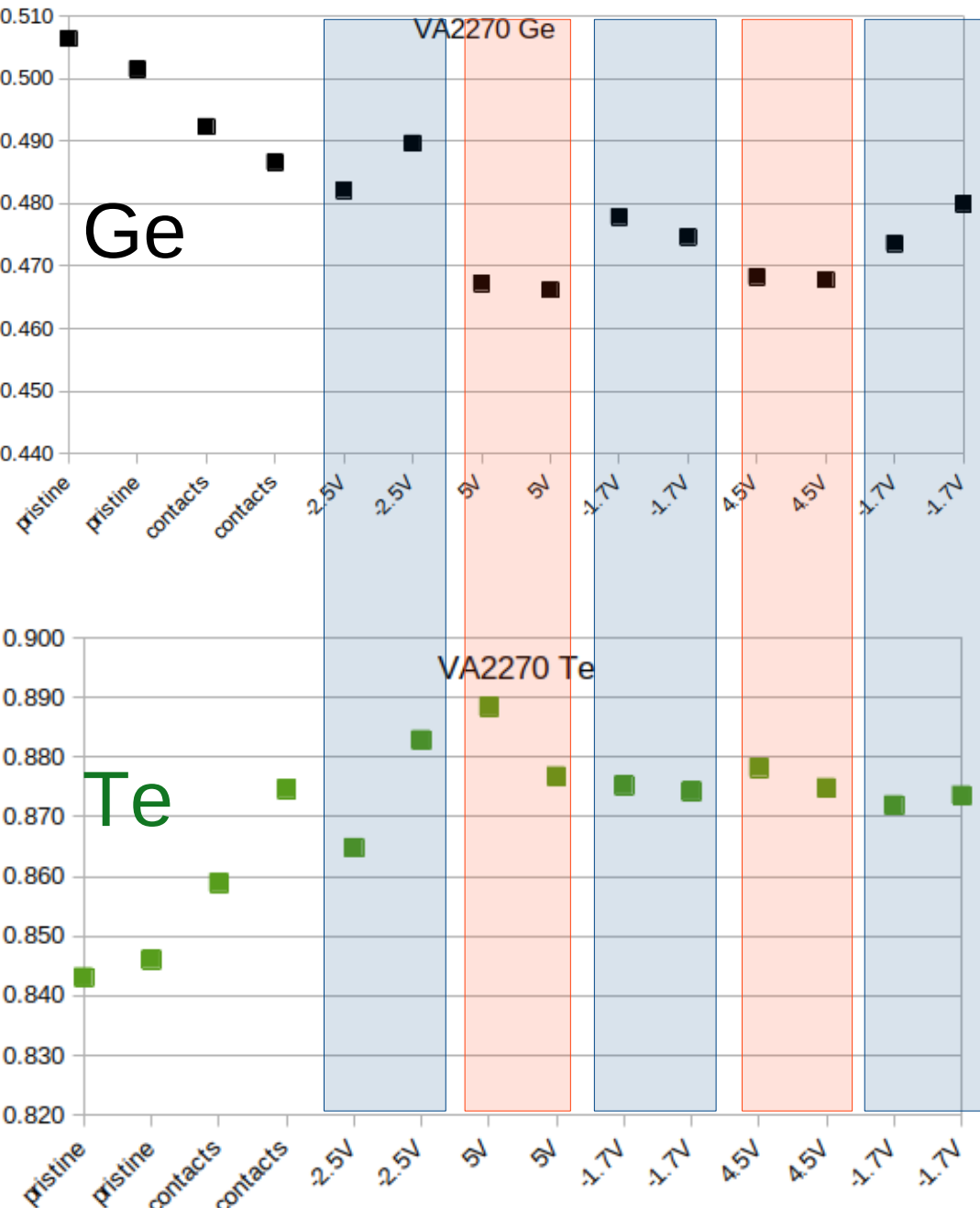
1.7 Å

1.4 Å or 2.0 Å

Fluorescence ve stojaté vlně



Standing waves in GeTe



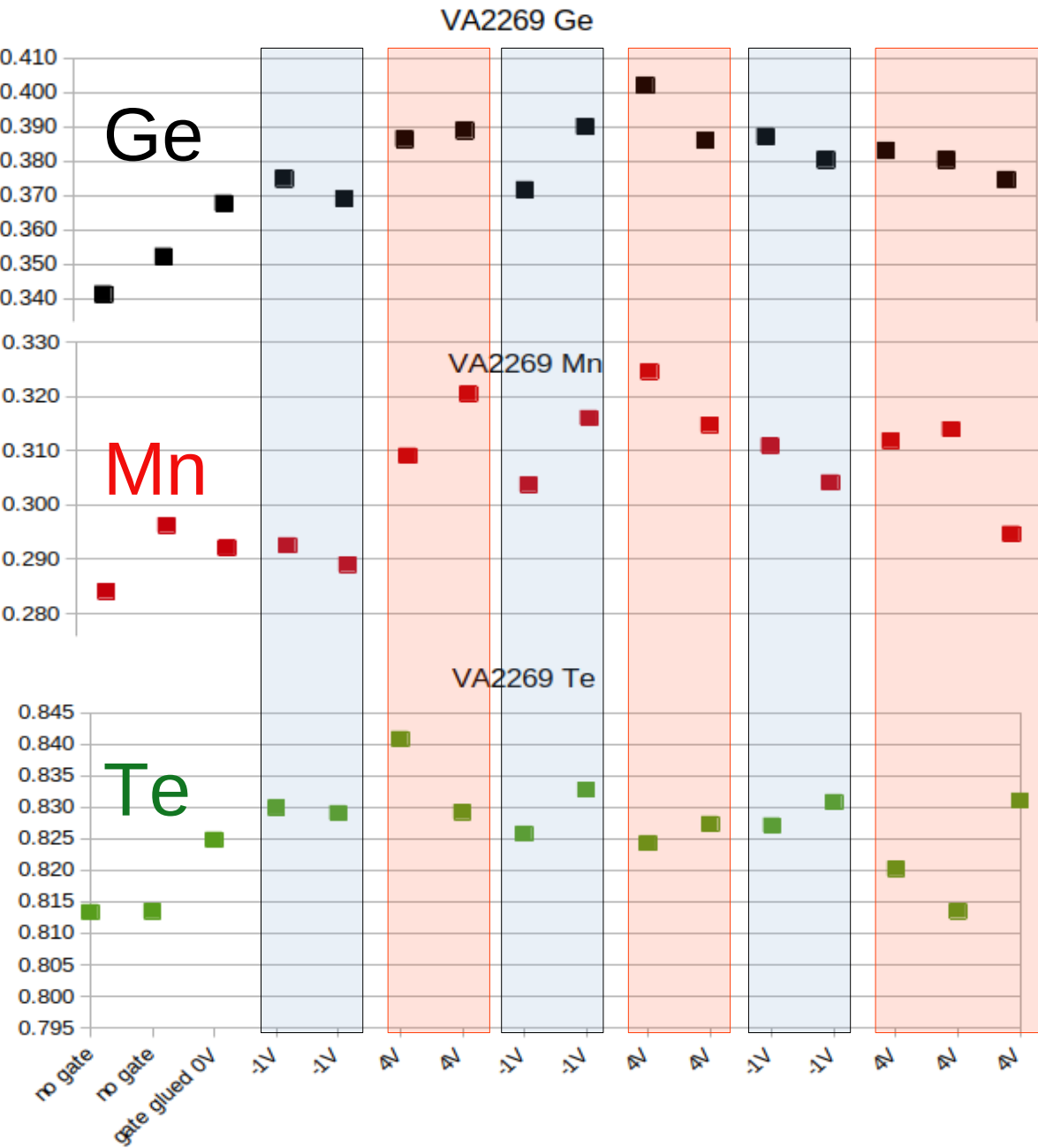
Atomic positions in fraction of standing wave period – InP (111) interplanar distance 3.39 Å

Only slight changes, very slow
No full switching

Shift of Ge position 0.06 Å

Red positive bias
Blue negative bias

Standing waves in (Ge,Mn)Te



Atomic positions in fraction of standing wave period – InP (111) interplanar distance 3.39 Å

Even smaller changes than in GeTe

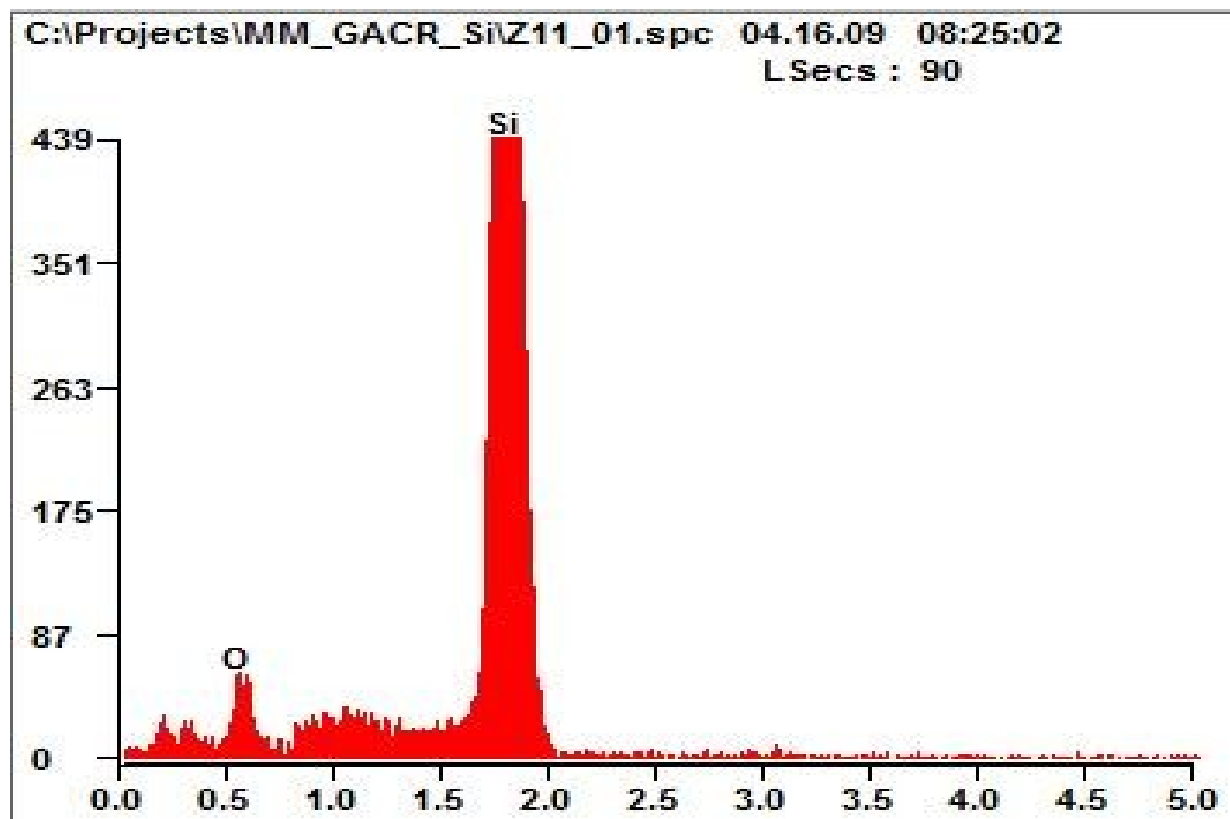
GeMnTe is closer to rocksalt structure.

Mn is close Ge position but shifted in average by 0.17 Å

Mn is in middle of Te positions – occupy cubic position

EDS, WDS

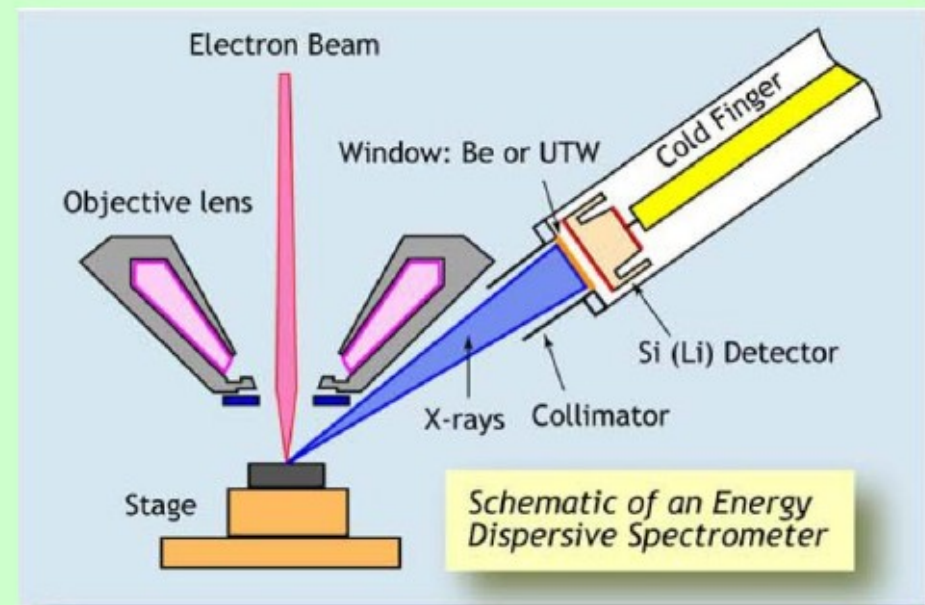
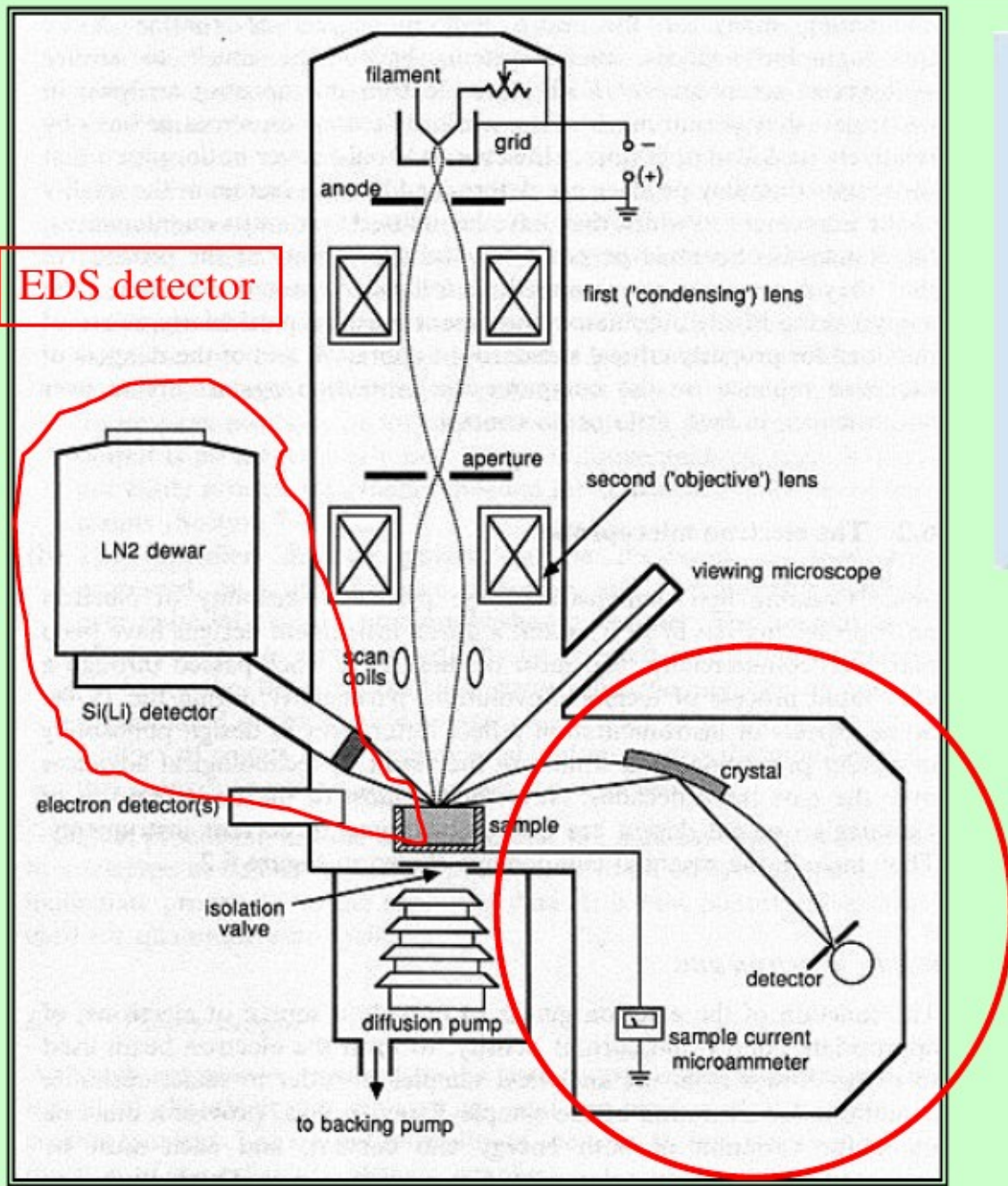
Energiově (vlnově) disperzní rentgenová spektroskopie
Energy Dispersive X-ray Spectroscopy – EDS (EDAXS)
Wavelength Dispersive X-ray Spectroscopy – WDS
Často s elektronovou mikroskopíí.
Lokální chemické složení vzorku. Povrchově citlivé.



Další podobné metody

PIXE – Particle Induced X-ray Emission – buzení iontovým svazkem

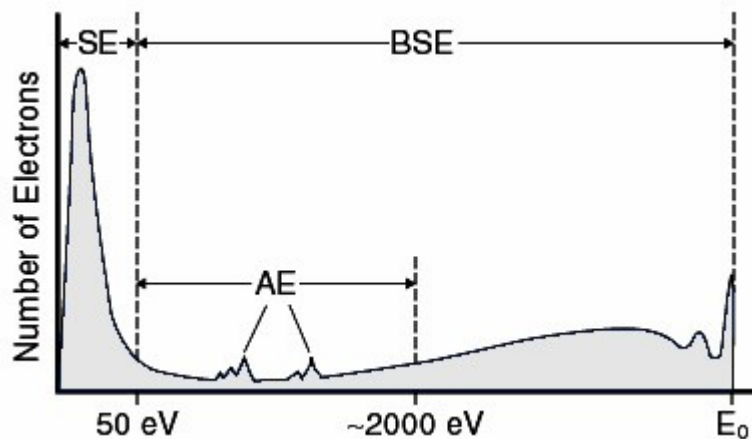
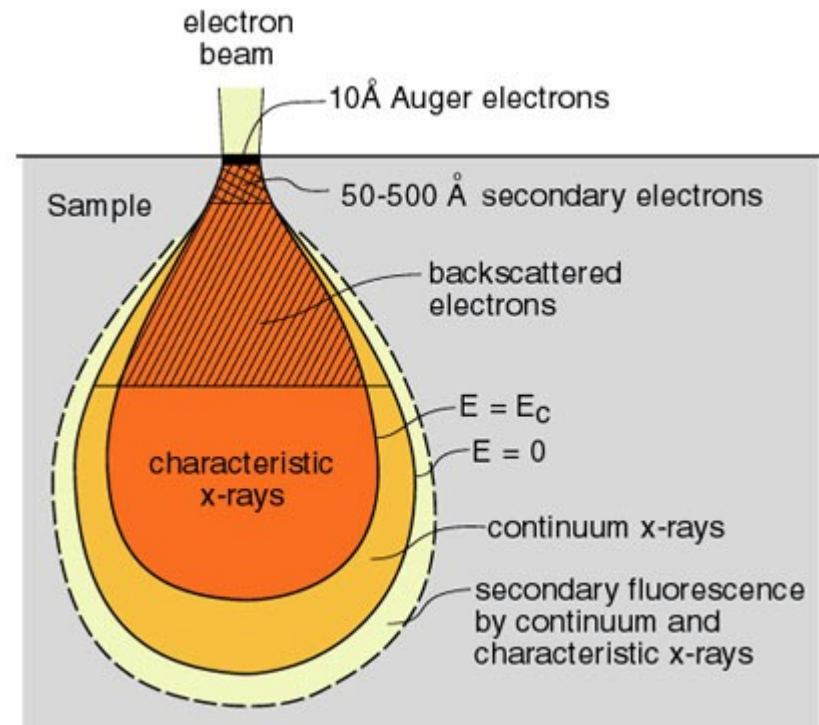
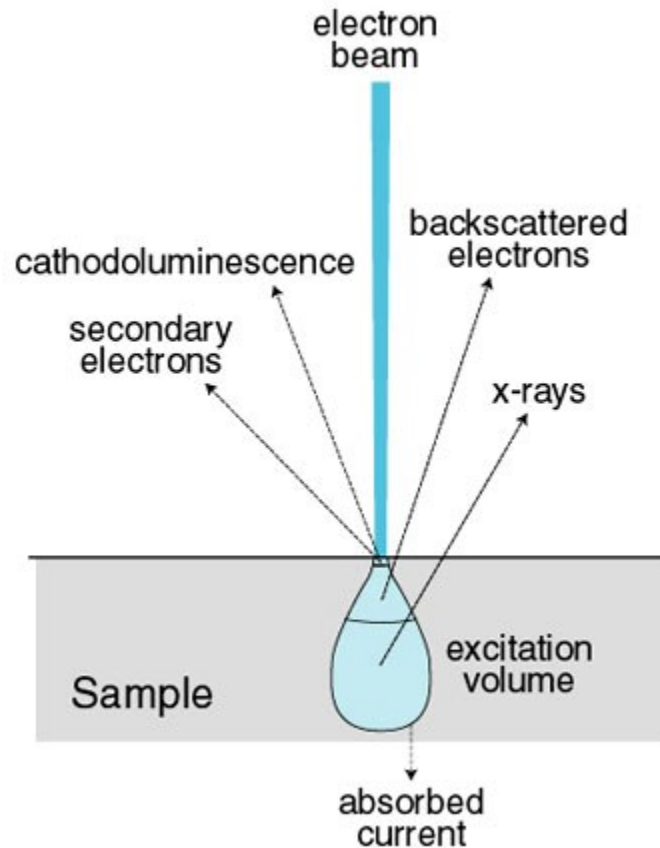
Electron microscopy



SEM combined with Energy dispersive spectrometer (EDS) and Wavelength Dispersive Spectrometer (WDS).

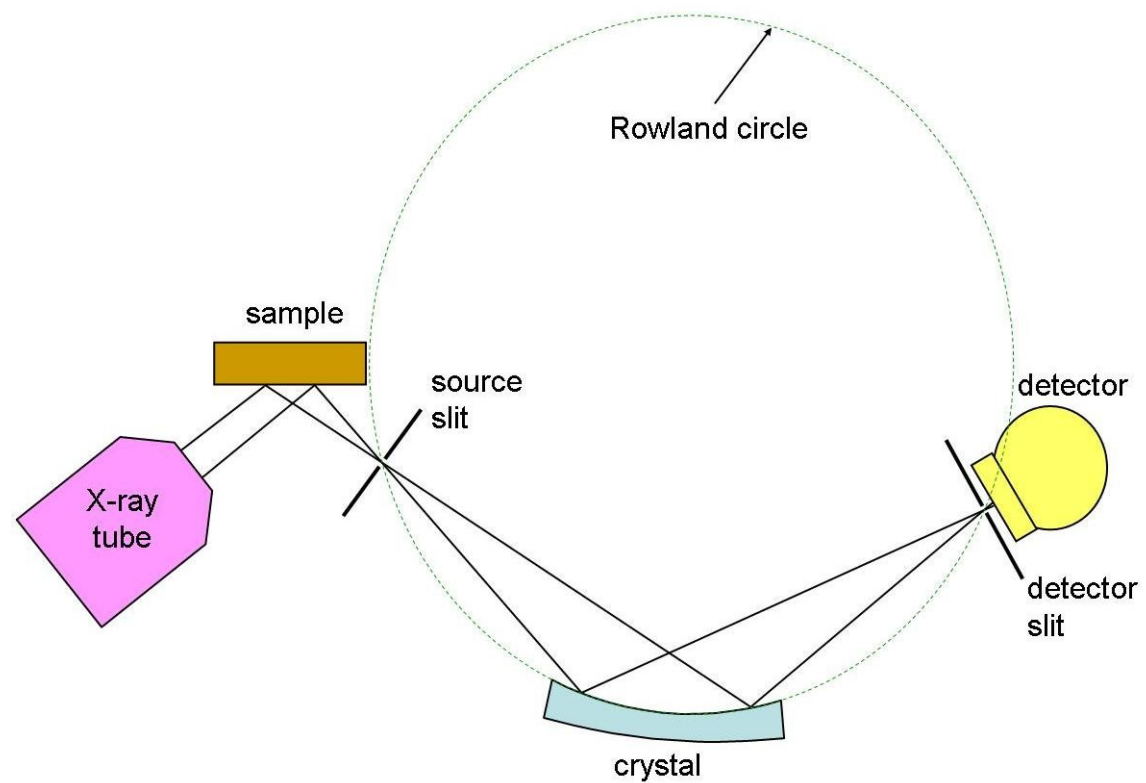
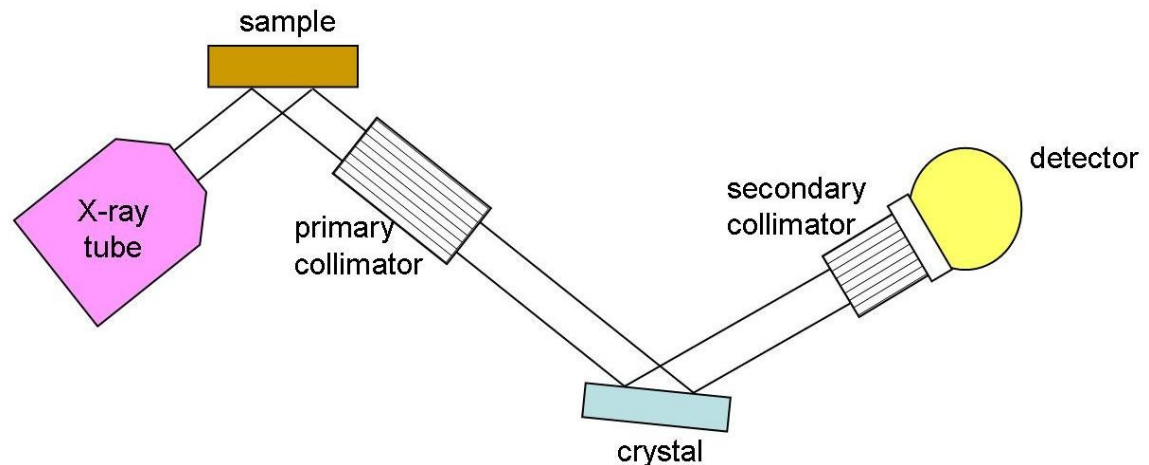
**WDS
spectrometers**

Electron microscopy



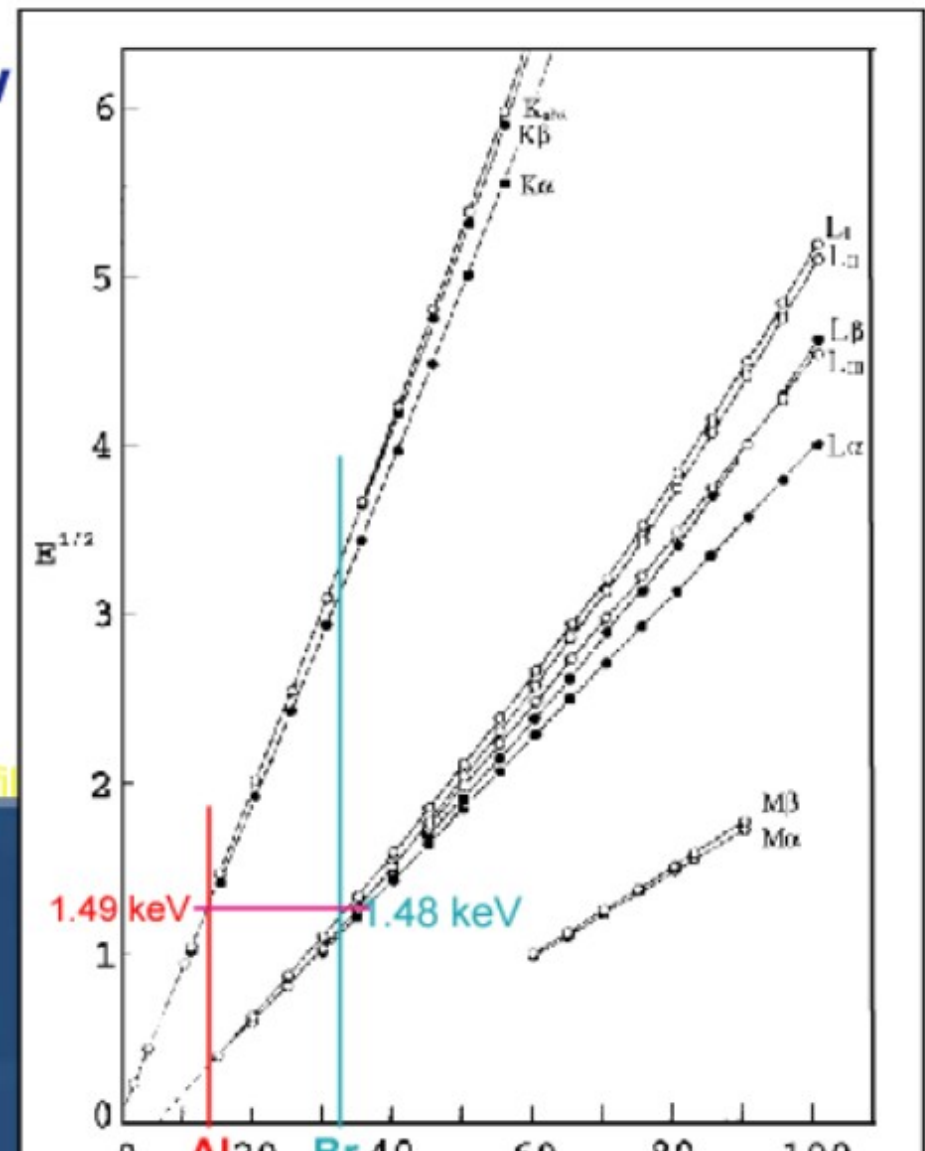
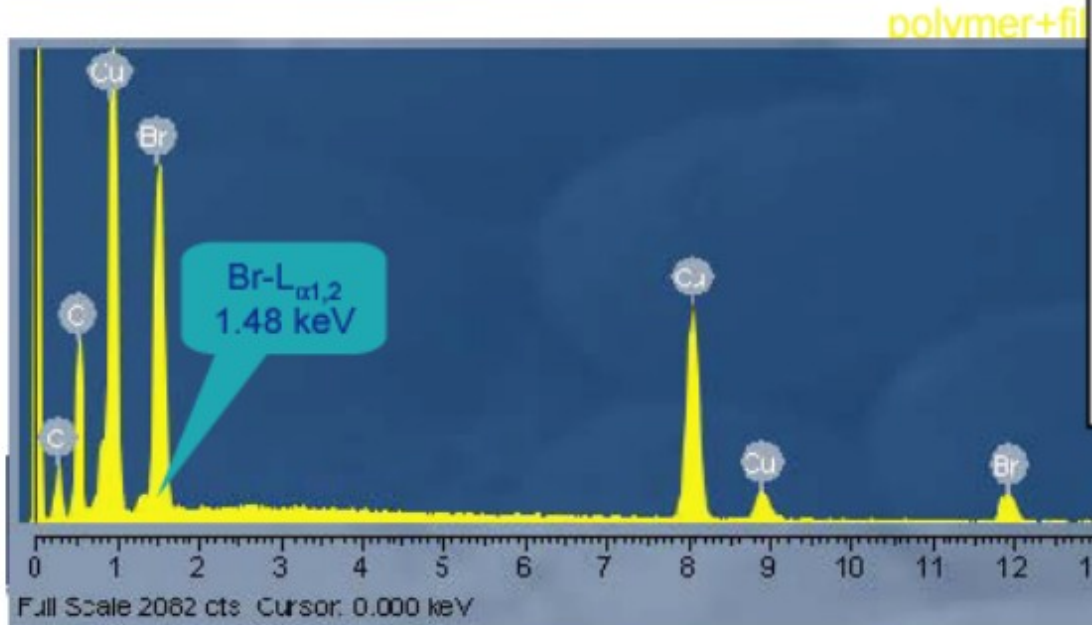
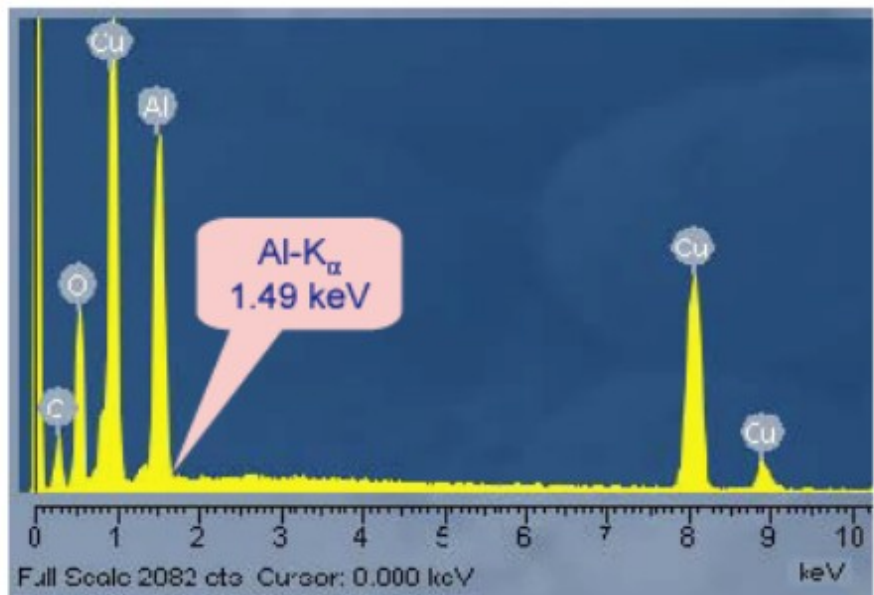
Electron microscopy

WDS:
better energy resolution
better precision
longer time



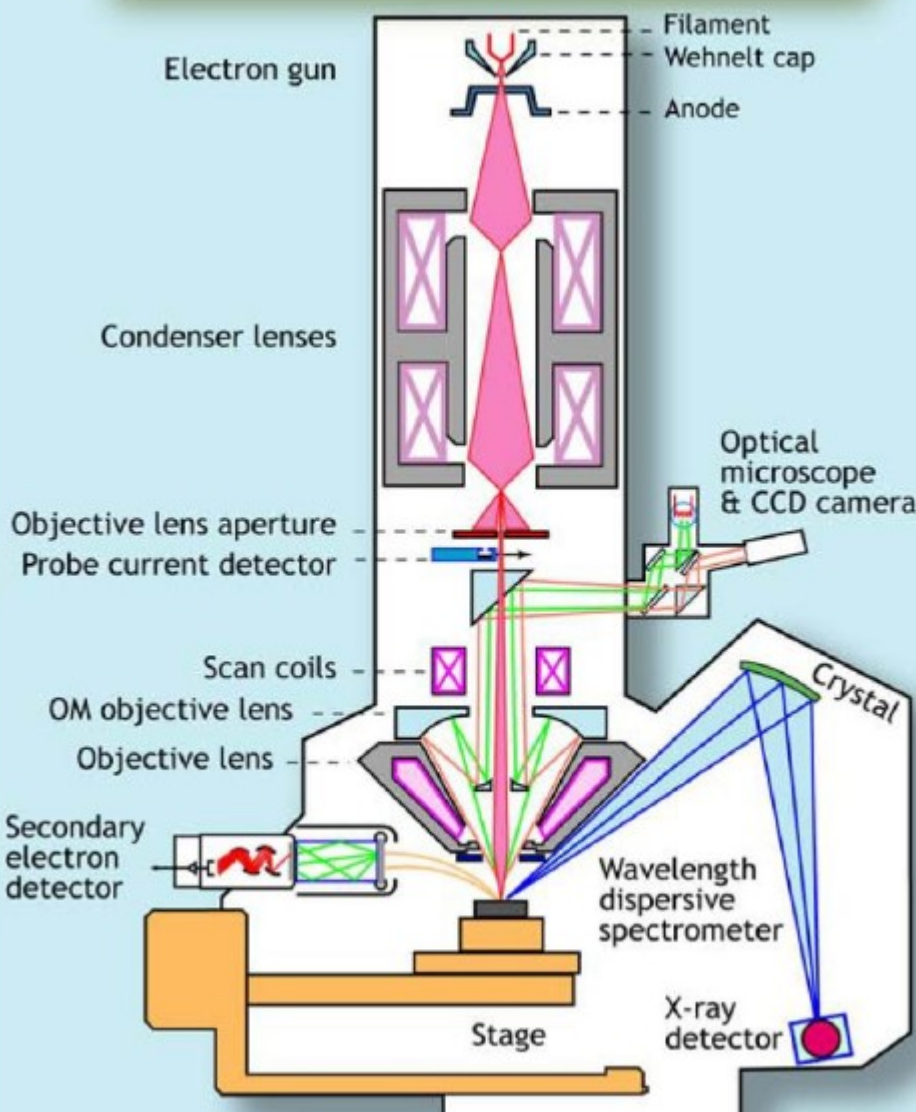
Electron microscopy

Characteristic lines: Moseley's Law

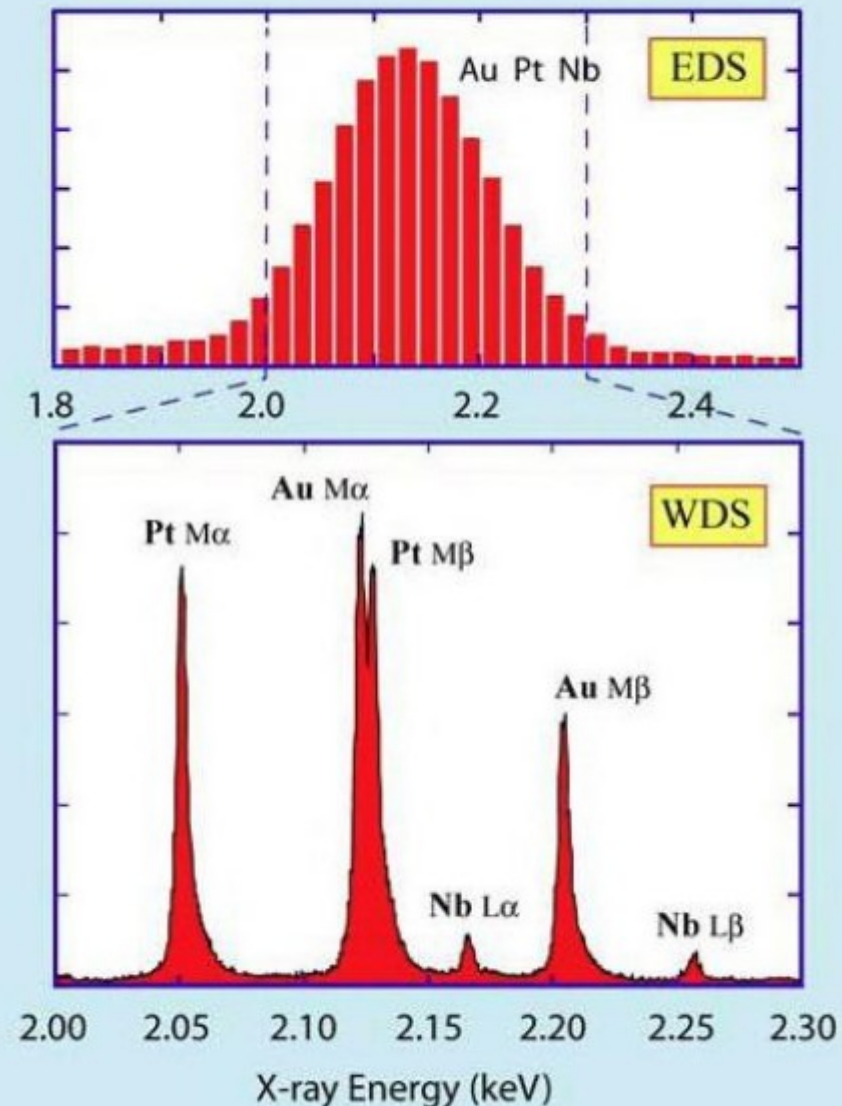


Electron microscopy

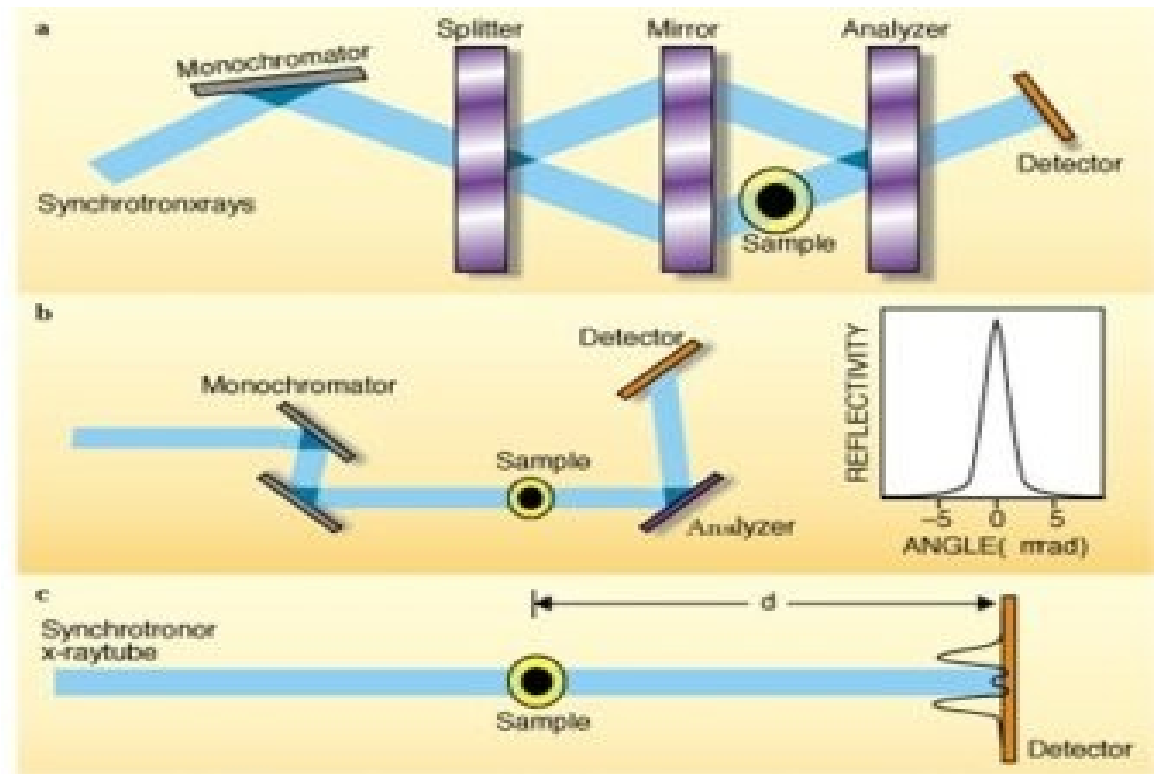
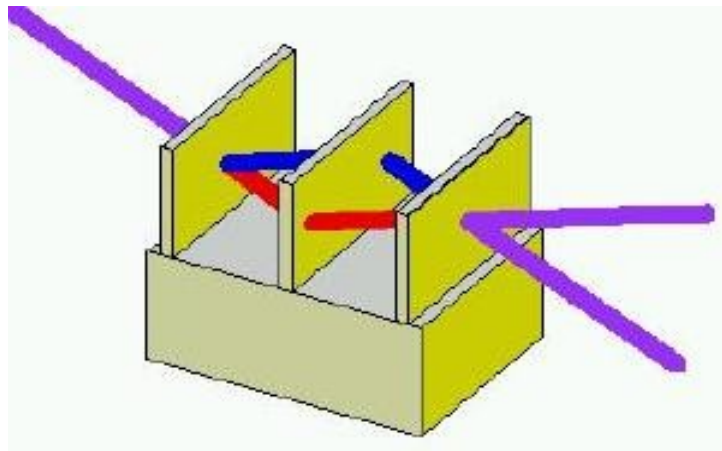
Schematic of an Electron Microprobe with a Wavelength Dispersive Spectrometer



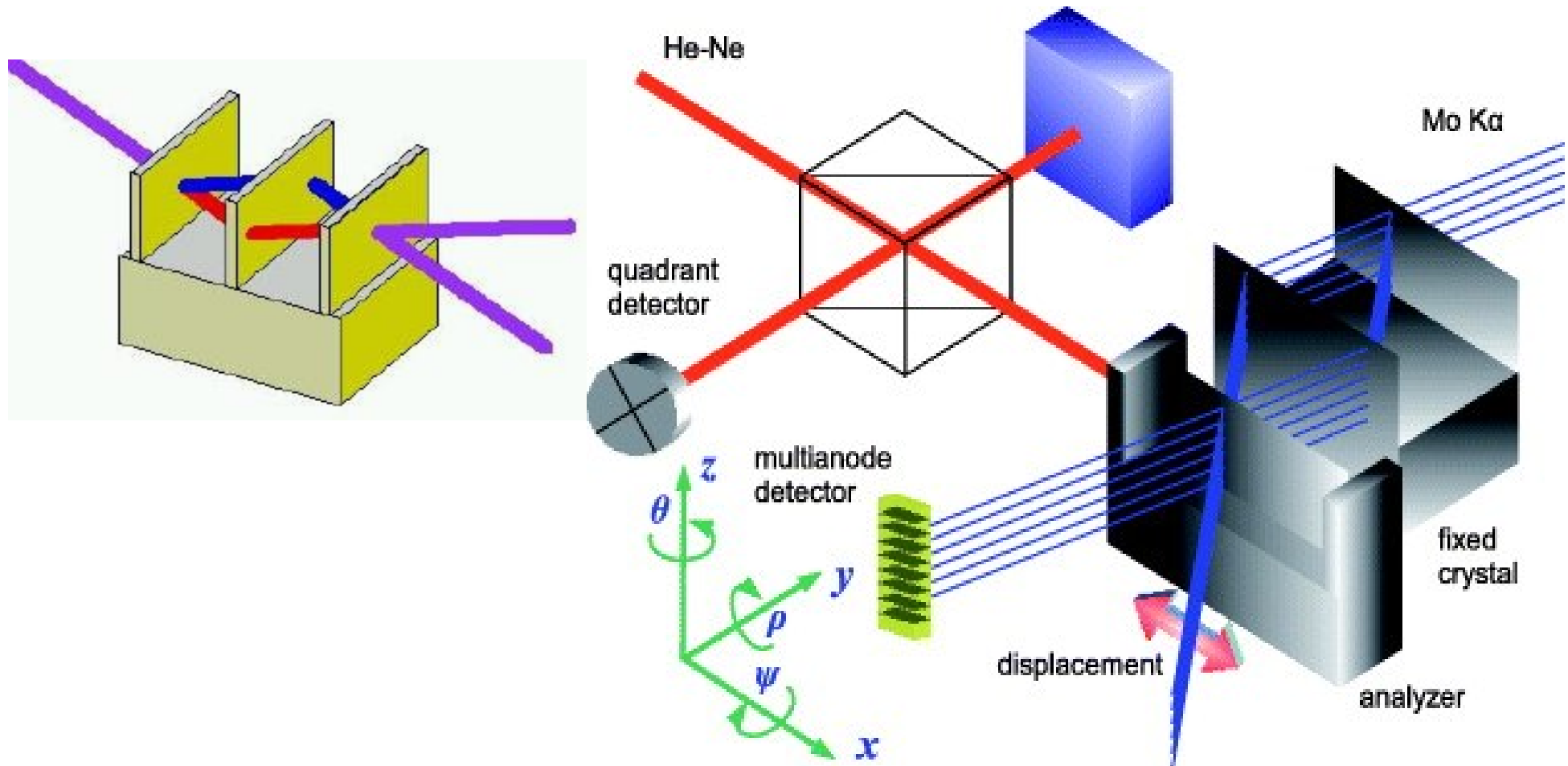
Energy Resolution of EDS vs WDS



Interferometrie



Interferometrie



Interferometrie

